POLITECNICO DI TORINO

UNIVERSITÄT STUTTGART

Master's Degree in Aerospace Engineering

Development of a model for the evaluation of the afterburning effect of rocket engines

Master Thesis from
Giacomo Corallo

University professors:
Prof. Domenic D'Ambrosio
Prof. Dr.-Ing. Stefanos Fasoulas

Supervisor:
Jan-Steffen Fischer
(Institute of Space System)

Dipartimento di Ingegneria Meccanica ed Aerospaziale
Institute of Space Systems

"Dare Mighty Things"

"A mamma, a papà, ad Alessio,
a tutta la mia famiglia,
a chi c'era, a chi c'è e a chi ci sarà"

Abstract

In the last decades, the number of orbital launches has significantly increased due to commercial, scientific, and technological motivations. As access to space becomes more frequent and affordable, the environmental impact of rocket emissions is gaining attention. However, the specific interactions between rocket exhaust plumes and the atmosphere, especially in terms of chemical reactions and pollutants formation, are still not completely understood. One of the key phenomena in this context is afterburning: the post-combustion of unburned species in the plume due to mixing with atmospheric gases.

This thesis presents the development of a simplified model aimed at studying the afterburning process in rocket plumes and estimating the resulting nitrogen oxide (NO) emissions. The model reproduces the structure of an under-expanded plume, divided into two regions: the inviscid core, where shock waves and expansion fans govern the flow, and the viscous mixing layer, where the turbulent interaction with the atmosphere allows for chemical reactions to occur.

The implementation includes the simulation of both regular and Mach reflection regimes, depending on altitude, and relies on the Reynolds-Averaged Navier-Stokes (RANS) equations with a $k - \epsilon$ turbulence model to solve the mixing layer behavior. The Chemical Equilibrium with Applications (CEA) tool is used to calculate the thermodynamic properties at the nozzle exit, while the NO formation is modeled through the Zeldovich mechanism and further reactions at the plume-atmosphere interface. Numerical methods based on finite differences and nonlinear least squares are used to solve the system in MATLAB.

Simulations are performed along a typical launch trajectory, and the influence of exit parameters such as temperature, pressure, density, Mach number, and nozzle diameter on NO production is analyzed. The results show how the shock structure, mixing intensity, and altitude strongly affect the temperature field and, consequently, the afterburning process. Furthermore, the study investigates the influence of the 11-year solar cycle on atmospheric density. A comparison between different engine architectures is also provided, showing their different environmental footprints.

The developed model, while simplified, provides valuable insights into the physics of rocket plumes and their impact on the upper atmosphere. It can be used as a tool to compare engine designs and support future studies on environmentally sustainable space transportation.

Contents

List of Figures

Nomenclature

Formula symbol

A	$\mathrm{m^3/(mol \cdot s)}$	Pre-exponential factor
A_p	-	Geomagnetic index
c_p	$\mathrm{J/(kg \cdot K)}$	Specific heat at constant pressure
c_v	$\mathrm{J/(kg \cdot K)}$	Specific heat at constant volume
C	$\mathrm{mol/m^3}$	Molar concentration
C_S	K	Sutherland constant
$e, \bar{e}, e'$	J/kg	Instantaneous, mean and fluctuating internal energy per mass unit
E_a	J/mol	Molar activation energy
$\mathrm{F}_{10.7}$	SFU	Solar radio flux at 10.7 cm
k	$\mathrm{m^2/s^2}$	Turbulent kinetic energy
$k(T)$	$\mathrm{m^3/(mol \cdot s)}$	Constant velocity
M	-	Mach number
M^*	kg/mol	Molar weight
n	-	Temperature exponent
$p, \bar{p}$	Pa	Instantaneous and mean pressure
P_k	$\mathrm{W/m^3}$	Turbulent kinetic energy production
q	$\mathrm{W/m^2}$	Conductive heat flux
s	$\mathrm{J/(K \cdot kg)}$	Specific entropy
S	$\mathrm{mol/(m^3 \cdot s)}$	Production rate
$T, \bar{T}, T'$	K	Instantaneous, mean and fluctuating temperature
T_S	K	Reference temperature
$u, \bar{u}, u'$	m/s	Instantaneous, mean and fluctuating velocity
w	-	Mass fraction

δ	rad	Mixing layer opening angle
δ'	-	Mixing layer opening angle tangent
ϵ	$\mathrm{m^2/s^3}$	Turbulent dissipation rate
γ	-	Ratio of the specific heats
μ, μ_t	$\mathrm{Pa \cdot s}$	Dynamic viscosity, turbulent dynamic viscosity
ν	$\mathrm{m^2/s}$	Cinematic viscosity
$\nu(M)$	rad	Prandtl-Meyer function
θ	rad	Angle between M_1 and M_2
θ_M	rad	Mach wave inclination
$\tau, \bar{\tau}$	$\mathrm{N/m^2}$	Instantaneous and mean viscous stress
ϕ	-	Interaction factor

Indices

0	Total variable
amb	Ambient
c	Chamber
e	Nozzle exit
i	Derivation direction
j, k	Chemical species
mix	Mixture
r	Reflection point

Constants

$C_{1\mu}$	1.44	Empirical constant of the ϵ equation
$C_{2\mu}$	1.92	Empirical constant of the ϵ equation
C_μ	0.09	Empirical constant of the $k-\epsilon$ model
k_b	$1.38 \times 10^{-23}\,\mathrm{J/K}$	Boltzmann constant
Pr_t	$0.85-0.9$	Turbulent Prandtl number
R	$8.314\,\mathrm{J/(mol\cdot K)}$	Gas constant
σ_k	1	Turbulent Schmidt number for k
σ_ϵ	1.3	Turbulent Schmidt number for ϵ

Abbreviations

CEA	Chemical Equilibrium with Applications
EUV	Extreme Ultraviolet
Fig.	Figure
LRE	Liquid Rocket Engine
MR	Mixture Ratio
NIST	National Institute of Standards and Technology
NOAA	National Oceanic & Atmospheric Administration
SRM	Solid Rocket Motor
Tab.	Table

1 Introduction

Since the beginning of the 21st century, the number of orbital launches has exponentially increased due to commercial, scientific and technological reasons, but also due to an increasing accessibility of space. Nowadays, rocket launches allow us to create new way of communication, for example through SpaceX Starlink project; new way of monitoring the Earth and the environment, like Copernicus project with Sentinel-1C satellite; new way of exploring and studying the universe, for instance Artemis program and the James Webb Space Telescope. In addiction, there are companies, such as Blue Origin and Virgin Galactic, that are offering a completely new service, possible thanks to definitely higher safety and reliability of rocket launches: space tourism.
The consequence of all these possibilities, as already mentioned, is an increase in the number of lift-off year by year, reaching almost 300 during 2024 and the prediction of doubling this value by 2029, as can be seen in Fig. 1.1.

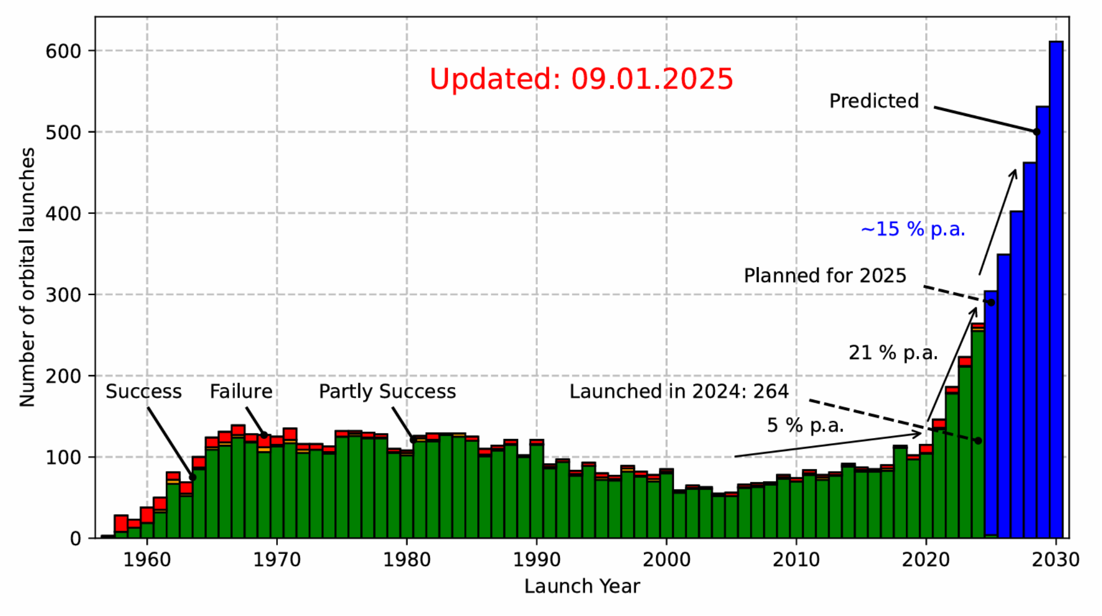

Figure 1.1: Number of launches per year [1]

With so many launches, greater attention must be paid to the environmental impact, which has not yet been properly studied in this case, leading to a lack of deep knowledge about the impact of rockets on our atmosphere and environment. In further details, when the exhaust plume exits a rocket nozzle, it undergoes complex interactions with the ambient atmosphere, producing well-known gas dynamic features such as Mach diamonds. At the jet boundaries, the mixing with atmospheric gases can lead to the afterburning of unburned fuel components and the formation of thermal nitrogen oxides (NO_x). These phenomena have so far received limited attention in scientific research.
This master's thesis aims to develop a dedicated model to describe and predict such afterburning processes. Following an initial review of the relevant literature, existing modeling strategies will be analyzed and compared. Based on this evaluation, a suitable model will be constructed to

simulate the afterburning phenomena. Widely used computational tools such as CEA will be integrated into the workflow. Eventually, the developed model will be used to perform simulations across a range of propellants, engine types, and atmospheric conditions.
This document consists on different Chapters, organized as follows: after the introduction part, where the problem is presented to the reader, a theoretical chapter is provided. Here, the main pollutants produced by the engines are presented with their effects on the atmosphere, an explanation of the plume structure and on how it depends on the altitude is included, as well as an explanation of the afterburning, main topic of the thesis. A chapter about the implemented model follows, where all the assumptions made and equations for the different phenomena used are exposed, along with the implementation in MATLAB. In the end, the results of the analysis are presented and discussed in details, with an explanation for the different graphs introduced about why the nitrogen oxides production changes with the different parameters.

2 Theoretical background

As reported by FASOULAS AND FISCHER [2], the impact of rocket emissions varies significantly with the type of propellant used, based on which we distinguish Solid Rocket Motor (SRM) or Liquid Rocket Engine (LRE), and with the design of the engine, which determines the development of the plume ([3]). In particular, liquid rockets that use carbon-based propellant produce soot, solid rockets with aluminum particles embedded in the propellant grain produce aluminum oxide Al_2O_3, also called alumina, and both of them produce nitrogen oxides NO_x.
An overview of the most important emissions from different propellants is shown in Tab. 2.1.

Propellants	Emissions
$Al/NH_4ClO_4 \pm$ HTPB (solid)	HCl, H_2O, CO_2, NO_x, Al_2O_3, soot
LO_x/LH_2	H_2O, H_2, OH, NO_x
N_2O_4/UDMH $\pm$ N_2H_4 (hypergolic)	H_2O, N_2, CO_2, NO_x, soot
LO_x/RP-1 (kerosene)	CO_2, H_2O, CO_x, OH, NO_x, soot

Table 2.1: Main emission products for different propellants. [3]

Let's see more in detail the pollutants previously cited.

2.1 Soot

Soot, also known as black carbon, consists of small, spherical carbon particles whose production depends on the mixture ratio of the engine and the combustion efficiency. In fact, normally liquid engines have a fuel-rich mixture ratio, leading to unmixedness that favors its production. The soot accumulates in the stratosphere, where it absorbs solar radiation and warms it, accelerating existing chemical reactions. [4]

2.2 Alumina

Alumina is the product of the melting of aluminum particles contained in the grain. The formation process begins with the combustion of the grain, followed by the melting of aluminum particles and their surface oxidation. This oxidation generates solid alumina, which then transitions to the liquid phase, forming liquid oxide particles. During this process, a growing blob that lately detaches develops as aluminum is consumed on the surfaces of the liquid particles. At the same time, smaller particles are blown off by the hot gas stream. As for soot, also alumina accumulates in the stratosphere, where it can remain up to 7 years, and it's under discussion the possibility that it warms the atmosphere up and favors chemical reactions, due to the fact that it reflects sunlight back to space. This leads also to the cooling of Earth's surface. [4]

2.3 Nitrogen oxide

Our atmosphere is composed for 78% of molecular nitrogen N_2. This nitrogen reacts with the high temperature exhaust plume, producing nitrogen oxides, such as nitric oxide NO, nitrogen dioxide NO_2 and nitrous oxide N_2O, which is then oxidized to NO_2 in the atmosphere. The first one is the most produced and, consequently, the most studied, and for it a principal mechanism of formation has been described, that is, thermal NO. Thermal NO is the most important source of NO in high temperature gas combustion, it's formed from oxidation of atmospheric nitrogen and consists in three reactions known as Zeldovich mechanism, highly dependent on temperature. It's important to notice this mechanism is appreciable for temperatures higher than 1800 K, being negligible under this value.

$N_2 + O \rightleftharpoons NO + N$
$N + O_2 \rightleftharpoons NO + O$
$N + OH \rightleftharpoons NO + H$

Table 2.2: Zeldovich mechanism

The first reaction is the one that requires more energy to start (Tab. 2.3), meaning that it's going to rule the entire mechanism velocity. [5, 6] The effect of nitrogen oxides on the atmosphere will be explained in the following Section.
The dependence on the temperature can be seen taking into account the Arrhenius equation

$$k(T) = AT^n \exp(-\frac{E_a}{RT}) \tag{2.1}$$

where A is the pre-exponential factor, E_a is the molar activation energy for the reaction, R is the universal gas constant, T is the absolute temperature and n is the temperature exponent. These values are empirical and have been found thanks to the Chemical Database of the *National Institute of Standards and Technology (NIST)*, which allowed to specify the parameters of the Arrhenius equation for forward and backward reactions. In the following Tables the parameters are presented

	A [m^3/mol/s]	E_a[kJ/mol]	n
$N_2 + O \longrightarrow NO + N$	1.81×10^8	318	0
$N + O_2 \longrightarrow NO + O$	9.03×10^3	27.2	1
$N + OH \longrightarrow NO + H$	2.83×10^7	0	0

Table 2.3: Forward Zeldovich reactions. [7]

	A [m^3/mol/s]	E_a[kJ/mol]	n
$NO + N \longrightarrow N_2 + O$	4.28×10^7	6.57	0
$NO + O \longrightarrow N + O_2$	6.88×10^2	160	1.13
$NO + H \longrightarrow N + OH$	2.17×10^8	207	0

Table 2.4: Backward Zeldovich reactions. [7]

The profile of the different $k(T)$ is showed in the following figure.

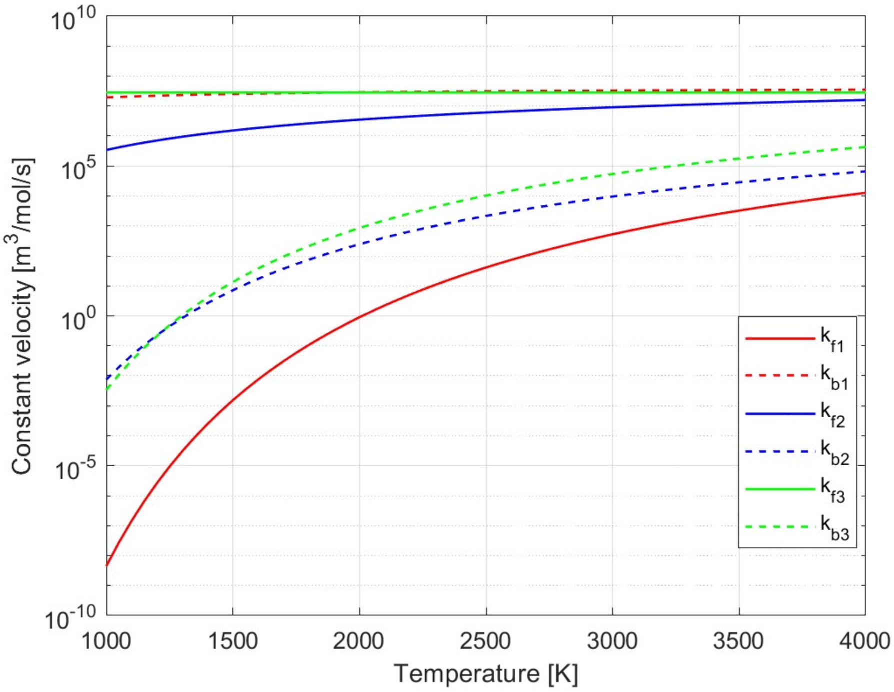

Figure 2.1: Trend of the different $k(T)$

As it's possible to notice, the Zeldovich mechanism is negligible under 1800 K since the values of the constant velocities $k(T)$ are too low for colder plumes, leading to a very low and not considerable NO production

2.4 Ozone depletion

Ozone O_3 is a gas that forms a layer in Earth's stratosphere, known as ozone layer, that protects the surface and life from ultraviolet (UV) radiation coming from the Sun, absorbing most of it. The ozone layer can be depleted by free radical catalysts, including nitrogen oxides NO_x, hydroxyl OH, chlorine Cl_x and bromine Br_x, present in nature but whose quantities in the stratosphere have been increased by human activities, resulting in the destruction of ozone molecules. For example, nitric oxide NO interacts with ozone with the following mechanism:

$$\mathrm{NO} + \mathrm{O_3} \longrightarrow \mathrm{NO_2} + \mathrm{O_2}$$
$$\mathrm{NO_2} + \mathrm{O} \longrightarrow \mathrm{NO} + \mathrm{O_2}$$

Usually, SRMs contain chlorine atoms that can generate HCl, which is later converted to the radical catalyst Cl_x in the plume. This reacts with the ozone, following the reaction:

$$\mathrm{Cl} + \mathrm{O_3} \longrightarrow \mathrm{ClO} + \mathrm{O_2}$$

Later, chlorine monoxide ClO can react with atomic oxygen, releasing a new chlorine atom

$$\mathrm{ClO} + \mathrm{O} \longrightarrow \mathrm{Cl} + \mathrm{O_2}$$

In this way, a loop that can destroy many ozone molecules from a single chlorine atom has begun. Another chemical species that leads to the ozone destruction is the already mentioned alumina Al_2O_3, which promotes the following reaction on its surface:

$$\mathrm{ClONO_2 + HCl \longrightarrow HNO_3 + Cl_2}\ [8]$$

Subsequently, the formed Cl_2, which is inert on itself, undergoes photodissociation due to UV radiation, producing two chlorine atoms that react with ozone, as explained above.

$$\mathrm{Cl_2 + h\nu \longrightarrow Cl + Cl}$$

This last reaction occurs only during daylight hours and can cause the loss of hundreds of ozone molecules.

Chlorine nitrate $ClONO_2$ is a gas formed in the stratosphere by the reaction between active chlorine ClO and nitrogen monoxide NO_2, whose job is to make less reactive these two chemical species.

As regards soot, it has an indirect effect to ozone depletion. In fact, it doesn't interact with it, but it accelerates the depletion process by warming up the stratosphere. [3, 2]

2.5 Plume structure

Plume phenomenology depends on the rocket engine and its basic configuration, with particular attention that must be paid to the combustion chamber and the nozzle. Combustion chamber is where the chemical reactions between oxidizer and fuel occur, releasing a high amount of energy that allows an increasing gas pressure and temperature. In LRE, oxidizer and fuel are contained in separate tanks and then mixed in the combustion chamber; in SRM, oxidizer and fuel are bonded at molecular or mechanical level, forming the so-called grain.

The high temperature and high pressure gas flows then in the de Laval nozzle, a convergent-divergent nozzle that rapidly accelerates it to a supersonic velocity. This implies a fast expansion of the post-combustion gas, with an increase of the gas volume and a decrease of the pressure. This pressure drop is very important for the behavior of the plume, which can be classified as over-expanded, under-expanded or perfectly expanded. In particular, the plume is over-expanded if the pressure at the nozzle exit is lower than the ambient pressure, under-expanded if it is higher, perfectly expanded if they are equal. Since the ambient pressure continuously decreases along the trajectory, the perfectly expanded condition is respected in a specific point of the trajectory, and from this point on the plume is going to be under-expanded. Depending on the type of plume, a different structure of shock waves and expansion fans will develop.

These three configurations are presented in Fig. 2.2.

2.5.1 Under-expanded plume

If an under-expanded condition has to be respected, the condition $p_\mathrm{e} > p_\mathrm{amb}$ must be verified, where p_e is the pressure at nozzle exit, p_amb is the ambient pressure. When this happens, the pressure gradient forces the gas to expand at the nozzle lip through an expansion fan, accelerating the flow and reducing the pressure until it reaches a value close to the ambient one. At this point, the gas will be compressed again, causing its pressure to rise, through elementary compression waves (Mach waves) that coalesce, forming an oblique shock wave. These elementary waves are generated from the reflection of the expansion waves from the expansion fan on the slipline, called free jet boundary, that formed between the plume itself and the atmosphere. Later, the oblique

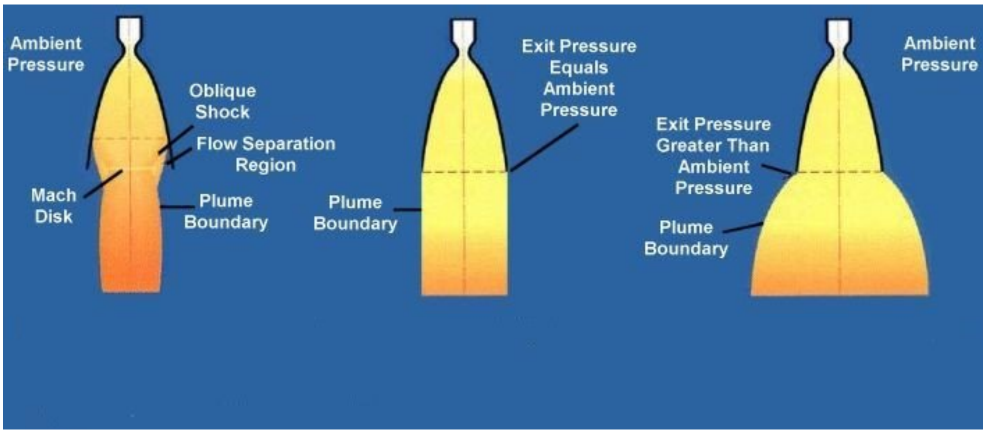

Figure 2.2: Over-expanded (left), perfectly expanded (center), under-expanded (right) plume [9]

shock wave is reflected in the centerline with a type of reflection that depends on the altitude: Mach reflection or regular reflection. In the case of a regular reflection, the reflected shock wave is another shock wave, while for Mach reflection a structure with the so-called Mach disc, a normal shock wave that forms in the plume centerline, develops. The oblique shock wave meets the Mach disc in a point called shock triple point, where it is reflected forming a third shock wave. In this way, the flow is comprised to a greater pressure than the ambient pressure, and the structure has gone back to a condition similar to the initial one. This means that the entire pattern is repeated downstream, creating the characteristic Mach diamond, although the dissipative effects will eliminate this structure at a certain point.

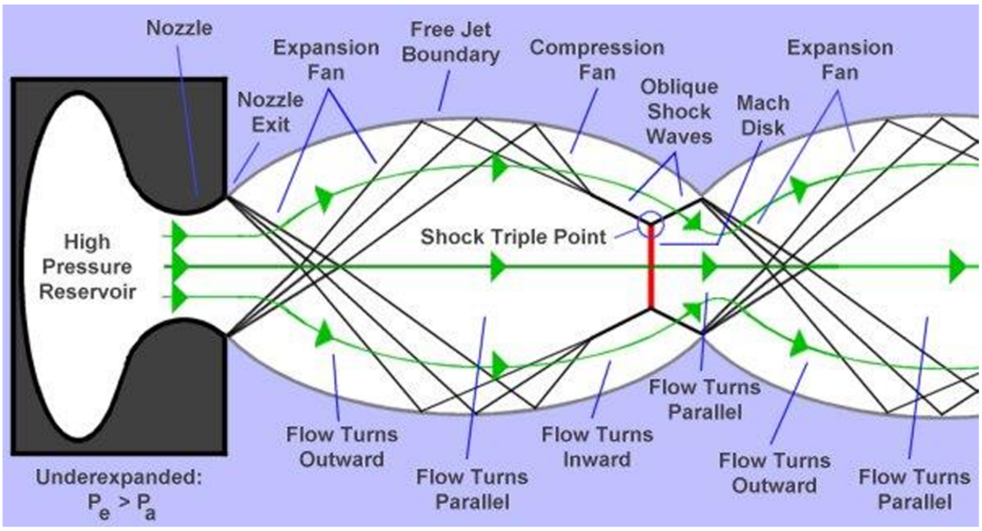

Figure 2.3: Under-expanded plume structure [10]

All these characteristics allow the division of the plume in two regions (Fig. 2.4): the inviscid core, where shock waves and expansion fans occur, regulating the flow structure; and the viscous mixing layer, where chemical reactions take place by mixing of the plume with the atmosphere during the afterburning. The viscous mixing layer grows as the plume extends downstream.
At the same time, three other regions can be identified: near field, transition region and far field (Fig. 2.5).

- Near field: close to the nozzle exit, here the mixing layer is very small and the flow velocity very high, leading to a mixing between plume and atmosphere negligible.

- Transition region: where the mixing with the atmosphere is not negligible anymore and the core flow becomes smaller and smaller.
- Far field: it begins where the Mach diamond structure no longer exists and the mixing with the atmosphere dominates, thanks to a high turbulence intensity. [11]

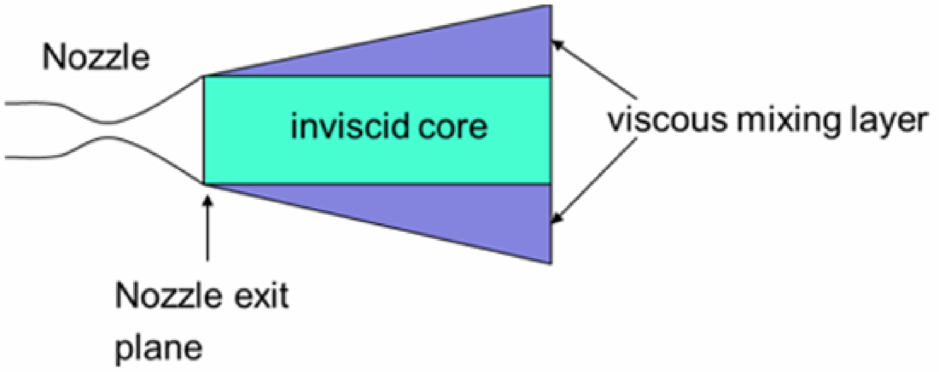

Figure 2.4: Plume structure in the near field [11]

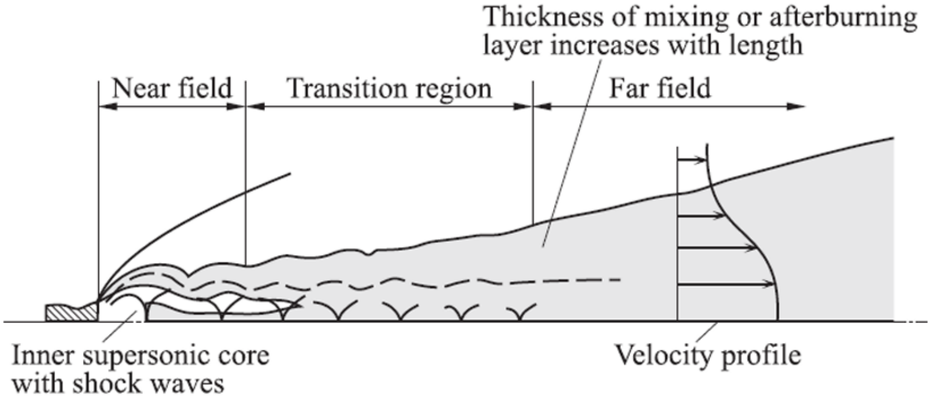

Figure 2.5: Division of the plume structure [2]

2.5.2 Over-expanded plume

Over-expanded plume is obtained when the pressure at the nozzle exit satisfies $p_{\mathrm{e}} < p_{\mathrm{amb}}$. In this condition, an oblique shock wave at the nozzle lip and a Mach disc downstream in the centerline are formed, compressing the flow in order to have a pressure similar to ambient pressure. The oblique shock wave meets the Mach disc in the triple point, being here reflected. After these compressions, the pressure raises to a higher value then the ambient pressure, leading to the formation of an expansion fan. From now on, the plume structure will be similar to the under-expanded plume one, with the formation of the Mach diamond.

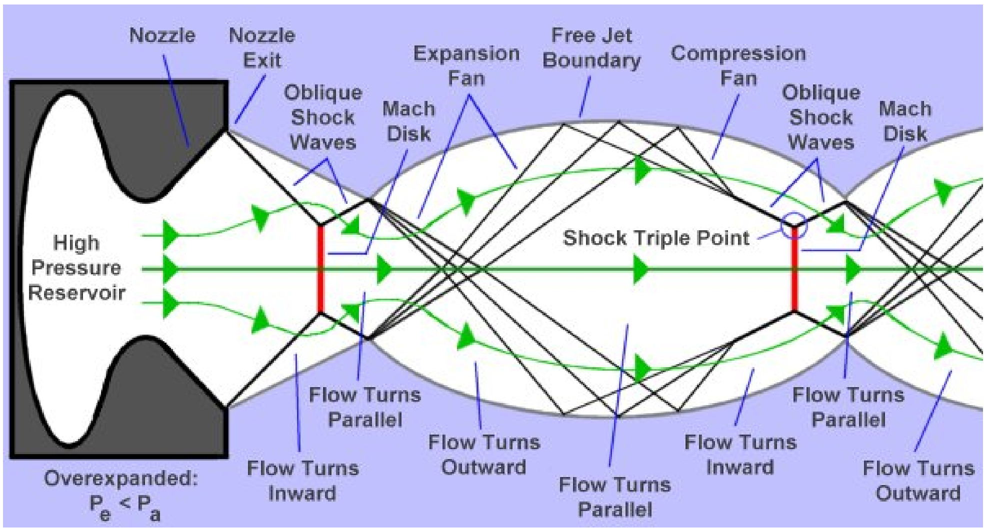

Figure 2.6: Over-expanded plume structure [10]

2.6 Afterburning

As already mentioned, the far field is dominated by the mixing layer and what happens in there. The high turbulence intensity favors the entrance of atmospheric oxygen inside the plume, leading to the so-called afterburning. Afterburning is a phenomenon characterized by the combustion of the unburned species present in the exhaust plume thanks to the interaction with the surrounding atmosphere, leading to very high temperature in the mixing layer. The unburned species are present due to the typical fuel-rich mixture ratio used in the rocket engine, useful for optimization of engine efficiency, reducing the combustion temperature (in order to protect combustion chamber and nozzle) and increasing combustion stability.

So, afterburning depends principally on two factors, degree of mixing and oxygen quantity, and this means that the process just occurs in particular conditions of altitude and velocity. Indeed, during the ascend through the atmosphere, the oxygen partial pressure, and so it's concentration, decreases and the combustion will be more and more difficult. At the same time, the rocket velocity increases. At the beginning, this velocity is less than the plume one, and this is important because the relative velocity gradient between the plume and the atmosphere generates the turbulence needed for the mixing. So, with the increase of rocket velocity this gradient drops, meaning a drop of the turbulence in the mixing layer, a less efficient mixing and less oxygen inside plume, leading to the ending of the afterburning when the two velocities match.

Particular attention must be paid to the soot. The afterburning leads in fact to the oxidation of it in the mixing layer, following the reaction

$$2\,\mathrm{C} + \mathrm{O_2} \longrightarrow 2\,\mathrm{CO}\ [12]$$

which is the dominant combustion mechanism that consumes the soot, increasing the mixing layer temperature by energy release. Then, carbon monoxide CO might oxidize again, if sufficient oxygen is present:

$$2\,\mathrm{CO} + \mathrm{O_2} \longrightarrow 2\,\mathrm{CO_2}$$

Moreover, not all soot particles will be oxidized, but only those with a not excessive diameter value and a sufficient residence time in the plume, which must be superior to the combustion time. The process also depends on the oxygen partial pressure, which determines the temperature reached

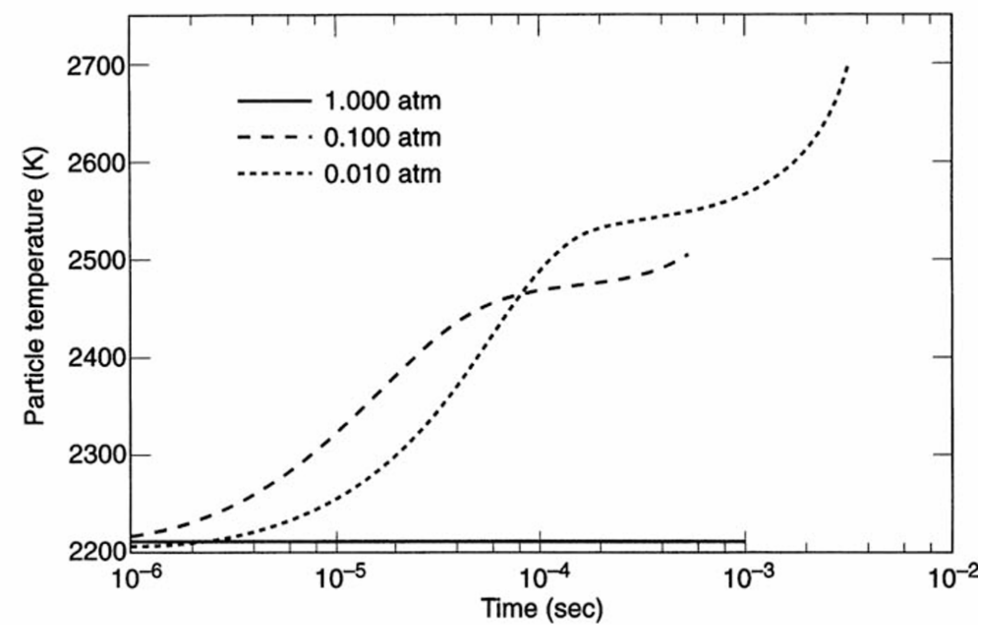

Figure 2.7: Soot particles temperature for various pressures of O_2 [13]

by the particles, as can be seen in Fig. 2.7. It is clear that a higher oxygen pressure favors a more efficient oxidation. [13]
The high mixing layer temperature caused by soot oxidation also favors a major NO production due to its strong dependency on high temperatures, with all the negative effects on the ozone layer already discussed in Section 2.4. In particular, the vortices created by the interaction between the plume and the atmosphere transport the fresh air inside the plume, to the boundary between the inviscid core and mixing layer. Here, the NO production is triggered.

3 Model

In the following chapter, the model implemented for the plume evolution is presented.
The model follows the plume structure described in the previous Chapter, including the development of the inviscid core, characterized by shock waves and expansion fans, and the viscous mixing layer, with the introduction of a turbulence model for the mixing with the atmosphere, following the three-region division illustrated in Fig. 2.5.
In addition, NASA's Chemical Equilibrium with Applications (CEA) software has been used to determine the flow conditions at the nozzle exit, which are fundamental for evaluating the flow evolution along the plume.
Some assumptions have been made, in particular for the inviscid core

- Steady 1D flow.
- Calorically perfect gas, a gas that obeys the ideal gas law with c_p and c_v independent from the temperature.
- Frozen composition.
- Laminar flow.
- No external forces.

For the mixing layer, instead

- Steady 2D flow.
- Calorically perfect gas.
- Equilibrium composition, considering that the combustion time is significantly shorter than the fluid dynamics time.
- Highly turbulent flow, requiring a turbulence model.
- Viscosity not negligible.

The governing equations are formulated in planar coordinates rather than in an axisymmetric framework. This choice simplifies the numerical implementation by avoiding the geometric $1/r$ terms and the associated singularity at the centerline.

3.1 Basic governing equations

The basic equations that rule the behavior of a laminar fluid are the continuity equation (3.1), the Navier-Stokes equations for the momentum (3.2) and the energy equation (3.3)

$$\frac{\partial(\rho u_i)}{\partial x_i} = 0 \tag{3.1}$$

$$\frac{\partial(\rho u_i u_j)}{\partial x_j} = -\frac{\partial p}{\partial x_i} + \frac{\partial \tau_{ij}}{\partial x_j} \tag{3.2}$$

$$\frac{\partial(\rho u_j c_v T)}{\partial x_j} = -\frac{\partial(p u_j)}{\partial x_j} + \frac{\partial(u_i \tau_{ij})}{\partial x_j} - \frac{\partial q_j}{\partial x_j} \tag{3.3}$$

with $\tau_{ij} = \mu \left(\frac{\partial u_i}{\partial x_j} + \frac{\partial u_j}{\partial x_i} \right)$ and $q_j = -k \frac{\partial T}{\partial x_j}$
In addition, the relations between total and static variables have been considered for the isentropic regions of the inviscid core, where all the viscous terms τ_{ij} are equal to 0. The isentropic relations are

$$\frac{p_0}{p} = \left(1 + \frac{\gamma - 1}{2} M^2 \right)^{\frac{\gamma}{\gamma - 1}} \tag{3.4}$$

$$\frac{T_0}{T} = 1 + \frac{\gamma - 1}{2} M^2 \tag{3.5}$$

$$\frac{\rho_0}{\rho} = \left(1 + \frac{\gamma - 1}{2} M^2 \right)^{\frac{1}{\gamma - 1}} \tag{3.6}$$

3.1.1 Transport properties

In the above equations, the parameters μ and k appear, which are respectively the dynamic viscosity, calculated through the Wilke formula for the gas mixture and Sutherland law for the single species

$$\mu_{\text{mix}} = \sum_{\text{j}=1}^{\text{n}} \frac{w_{\text{j}} \mu_{\text{j}}}{\sum_{\text{k}=1}^{\text{n}} w_{\text{k}} \phi_{\text{jk}}} \tag{3.7}$$

$$\mu_{\text{j}} = \mu_{0,\text{j}} \left(\frac{T}{T_{S,\text{j}}} \right)^{3/2} \frac{T_{S,\text{j}} + C_{S,\text{j}}}{T + C_{S,\text{j}}} \tag{3.8}$$

and the thermal conductivity of the gas, through the gas kinetic theory for a gas mixture

$$k_{\text{mix}} = \sum_{\text{j}=1}^{\text{n}} w_{\text{j}} \left(1.5 \frac{R}{M_{\text{j}}^*} \sqrt{\frac{8 k_b T}{\pi M_{\text{j}}^*}} \right) \tag{3.9}$$

where $\phi_{\text{jk}} = \frac{1}{\sqrt{8}} \left(1 + \frac{\mu_{\text{j}}}{\mu_{\text{k}}} \sqrt{\frac{M_{\text{k}}^*}{M_{\text{j}}^*}} \right)^{-1} \sqrt{1 + \frac{M_{\text{j}}^*}{M_{\text{k}}^*}}$ is the interaction factor, w is the mass fraction of the species j, T_S is the reference temperature, C_S is the Sutherland constant, M^* is the molar weight and $k_b = 1.38 \cdot 10^{-23}$J/K is the Boltzmann constant.

3.2 Supersonic phenomena

Thanks to the de Laval nozzle, the gas produced by the engine reaches supersonic velocities. On this, the behavior of the inviscid core is based, with the different characteristic phenomena that respect specific theories.

3.2.1 Expansion fans

An expansion fan is an isentropic process where a deflecting flow moves away with respect to the direction of the upstream flow. It is characterized by a continuous deflection through elementary expansion waves originated by a point of geometric discontinuity, each of them inclined of $\theta_M = \arcsin(\frac{1}{M})$ and causing infinitesimal variation of the flow parameters without energy dissipation. Being an expansion, this fan leads to an increase of the flow Mach number and a pressure, temperature and density drop.

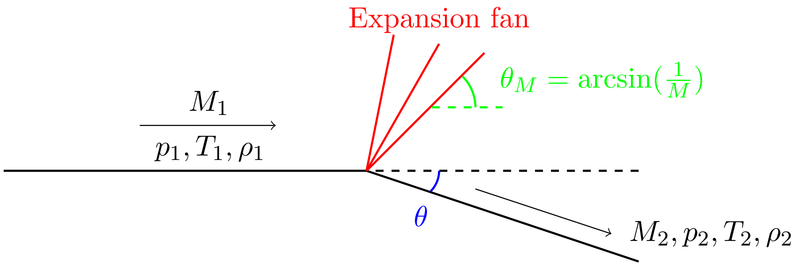

Figure 3.1: Expansion fan

The expansion fans can be studied through the Prandtl-Meyer theory. According to it, M_1 and M_2 can be related thanks to θ using the so-called 'Prandtl-Meyer function' $\nu(M)$, defined as

$$\nu(M) = \int \frac{\sqrt{M^2 - 1}}{1 + \frac{\gamma-1}{2}M^2} \frac{dM}{M} \tag{3.10}$$

whose solution is

$$\nu(M) = \frac{\sqrt{\gamma+1}}{\sqrt{\gamma-1}} \arctan\left(\sqrt{\frac{\gamma-1}{\gamma+1}}\sqrt{M^2-1}\right) - \arctan\left(\sqrt{M^2-1}\right) \tag{3.11}$$

At this point, it's possible to obtain the fundamental relation

$$\theta = \nu(M_2) - \nu(M_1) \tag{3.12}$$

with θ that must be positive for an expansion.
Once $\nu(M_2)$ has been established, M_2 can be calculated through numerical methods or using existing tables.
The parameters after the fan can be then evaluated through the following relations

$$\frac{T_2}{T_1} = \frac{1 + \frac{\gamma-1}{2}M_1^2}{1 + \frac{\gamma-1}{2}M_2^2} \tag{3.13}$$

$$\frac{p_2}{p_1} = \left(\frac{1 + \frac{\gamma-1}{2}M_1^2}{1 + \frac{\gamma-1}{2}M_2^2}\right)^{\frac{\gamma}{\gamma-1}} \tag{3.14}$$

$$\frac{\rho_2}{\rho_1} = \frac{p_2}{p_1}\frac{T_1}{T_2} \tag{3.15}$$

3.2.2 Shock waves

Shock waves can be defined as discontinuity of the flow field parameters. In particular, along a streamline that crosses a shock wave, there is a sudden decrease of the Mach number and an increase of pressure, temperature and density. In addition, the process is extremely dissipative as a result of the strong velocity gradient across the shock, leading to a total pressure loss and an increase in entropy.
It's possible to distinguish different kinds of shock waves, but for the 1D flow configuration of the inviscid core there are normal (Fig. 3.2) and oblique shock waves (Fig. 3.3).

The flow behavior on the cusp of the shock wave can be determined through the so-called Rankine-Hugoniot relations, which are useful for calculating the parameters jump. Considering that the

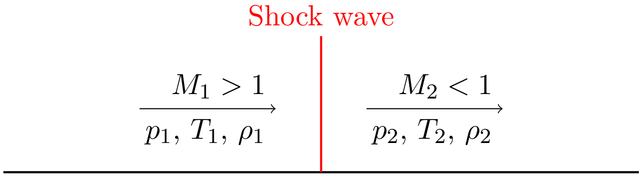

Figure 3.2: Normal shock wave

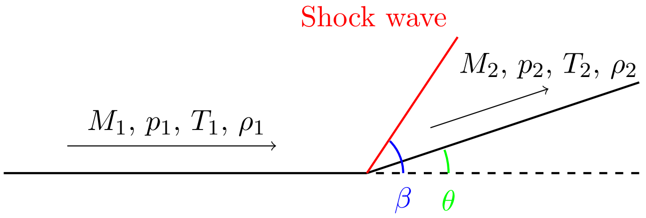

Figure 3.3: Oblique shock wave

subscript 1 indicates the before-shock parameters and 2 the post-shock parameters, these relations are the following:

$$M_2^2 = \frac{1}{\sin^2(\beta - \theta)} \left[\frac{2 + (\gamma - 1) M_1^2 \sin^2 \beta}{2\gamma M_1^2 \sin^2 \beta - (\gamma - 1)} \right] \tag{3.16}$$

$$\frac{p_2}{p_1} = 1 + \frac{2\gamma}{\gamma + 1} \left(M_1^2 \sin^2 \beta - 1 \right) \tag{3.17}$$

$$\frac{T_2}{T_1} = \left[1 + \frac{2\gamma}{\gamma + 1} \left(M_1^2 \sin^2 \beta - 1 \right) \right] \left[\frac{(\gamma - 1) M_1^2 \sin^2 \beta + 2}{(\gamma + 1) M_1^2 \sin^2 \beta} \right] \tag{3.18}$$

$$\frac{\rho_2}{\rho_1} = \frac{(\gamma + 1) M_1^2 \sin^2 \beta}{(\gamma - 1) M_1^2 \sin^2 \beta + 2} \tag{3.19}$$

$$\frac{p_{02}}{p_{01}} = \left[1 + \frac{2\gamma}{\gamma + 1} \left(M_1^2 \sin^2 \beta - 1 \right) \right]^{-\frac{1}{\gamma - 1}} \left[\frac{(\gamma + 1) M_1^2 \sin^2 \beta}{(\gamma - 1) M_1^2 \sin^2 \beta + 2} \right]^{\frac{\gamma}{\gamma - 1}} \tag{3.20}$$

$$s_2 - s_1 = -\frac{R}{M} \ln \left(\frac{p_{02}}{p_{01}} \right)$$

where M_1 and M_2 are the Mach numbers before and after the shock wave, θ is the angle between M_1 and M_2, β is the shock wave angle, γ is the specific heat-ratio of the gas. In particular, these formulae are for an oblique shock wave. The normal shock waves relations can be easily obtained imposing $\beta = 90°$ and $\theta = 0°$.

For oblique shock waves, another fundamental relation between θ, β and M_1 is required. This is

$$\tan \theta = \frac{2}{\tan \beta} \left[\frac{M_1^2 \sin^2 \beta - 1}{M_1^2 (\gamma + \cos 2\beta) + 2} \right] \tag{3.21}$$

For every Mach number, the minimum value of β is $\arcsin(\frac{1}{M_1})$ and the maximum is $\beta = 90°$, that is the normal shock wave.

In Fig. 3.4 the behavior of the relation (3.21) is presented.

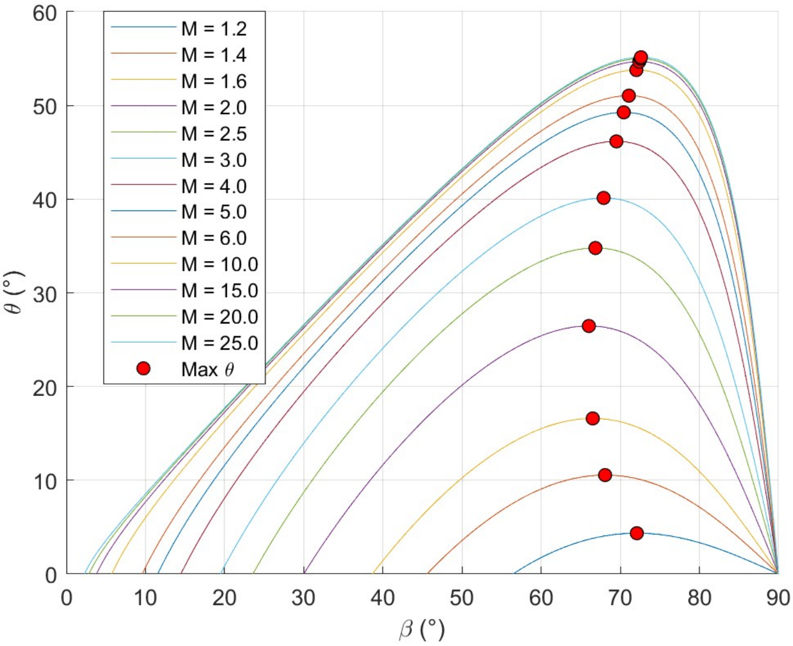

Figure 3.4: θ - β - M relation

It's important to notice the fact that higher the Mach number is, more intense the shock wave is, leading to an higher pressure, temperature and density jump, and an after-shock Mach number that tends to reach a limit value determined as $\sqrt{\frac{\gamma-1}{2\gamma}}$ (Fig. 3.5).

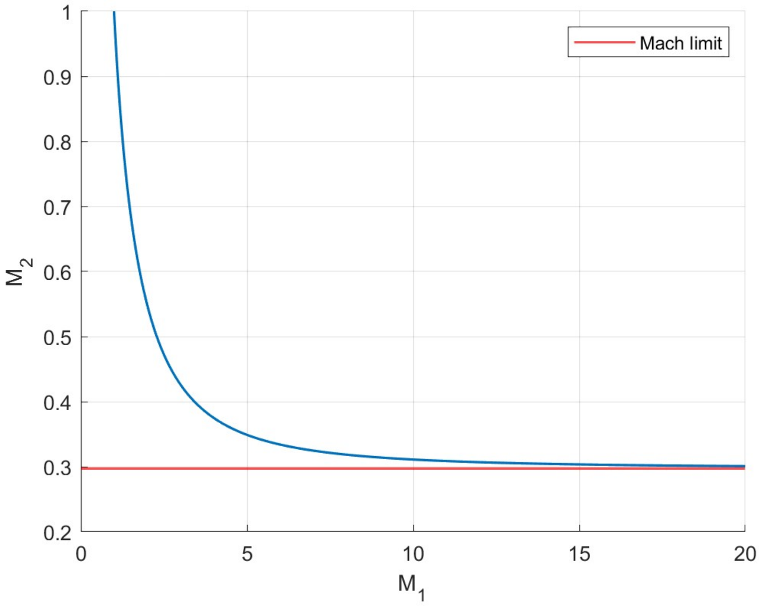

Figure 3.5: Variation of M_2 with M_1 for $\gamma = 1.21$

At the same time, following the relation θ - β - M with constant deflection angle, a higher Mach number can lead to either a more inclined shock and a less inclined shock, depending on the fact that the shock is respectively strong ($M_2 < 1$) or weak ($M_2 > 1$).

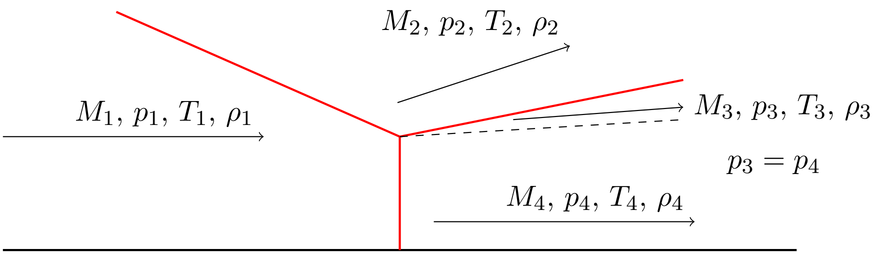

Figure 3.6: Mach reflection

3.2.3 Shock waves reflection

In the inviscid core, if the plume is symmetric, the centerline can be considered as a wall, leading to the fact that when two shock waves of different families meet there, a shock reflection that can be regular reflection or Mach reflection occurs.
Mach reflection (Fig. 3.6) occurs when the deflection angle θ required to turn the flow back to a direction parallel to the wall, after the incident shock, exceeds θ_{max} for M_2, meaning that the flow requires a deflection angle that's not physically achievable. This brings the system to develop Mach reflection, where the shock structure consists of three shocks: the incident shock, the reflected shock and a Mach stem, which is a normal shock wave. These meet in a point known as 'triple point'. It's important the fact that the pressure downstream the Mach disc and downstream the reflected shock are the equal, thanks to the existence of a slipline. This is necessary, since otherwise there would be vertical pressure gradient that would create a vertical velocity component.

At this point, it becomes fundamental evaluating the shock angle of the reflected shock wave, that must be such as to guarantee a post-oblique shock pressure equals to the post-Mach stem pressure, in order to avoid vertical pressure gradient that would not allow the flow to realign with the wall and would require additional expansion or compression waves. In order to do so, a shock polar is required. A shock polar is a graph which helps to calculate the reflected shock parameters representing how the pressure jump changes with the deflection angle for a fixed Mach number. So, for obtaining the reflected shock deflection angle, what has to be done is:

1. Plot the shock polar for M_1.
2. Determine M_2.
3. Plot the associated shock polar in the same coordinate system.
4. The intersection between the two shock polar provides the deflection angle of the reflected shock.

An example result of this process is presented in Fig. 3.7.
The minimum θ is the one associated with $\theta_M = \arcsin(\frac{1}{M})$, while the lowest point of second shock polar is the real pressure jump across the incident shock.
Regular reflection (Fig. 3.8) occurs instead when $\theta < \theta_{max,M_2}$, so the flow is capable of realigning with the wall, leading to the regular reflection condition

$$\theta_1 + \theta_2 = 0$$

Furthermore, the type of reflection depends on the altitude and, in particular, on the nozzle exit pressure-to-ambient pressure ratio. In fact, a higher $p_\mathrm{e}/p_\mathrm{amb}$ (corresponding to a lower p_amb) triggers a less inclined shock wave. As a result, the flow crosses the shock waves farther from the nozzle exit. Therefore, as the altitude increases, the reflection point and, in general, the entire shock waves structure, moves downstream, resulting in a faster flow. As a consequence, a higher

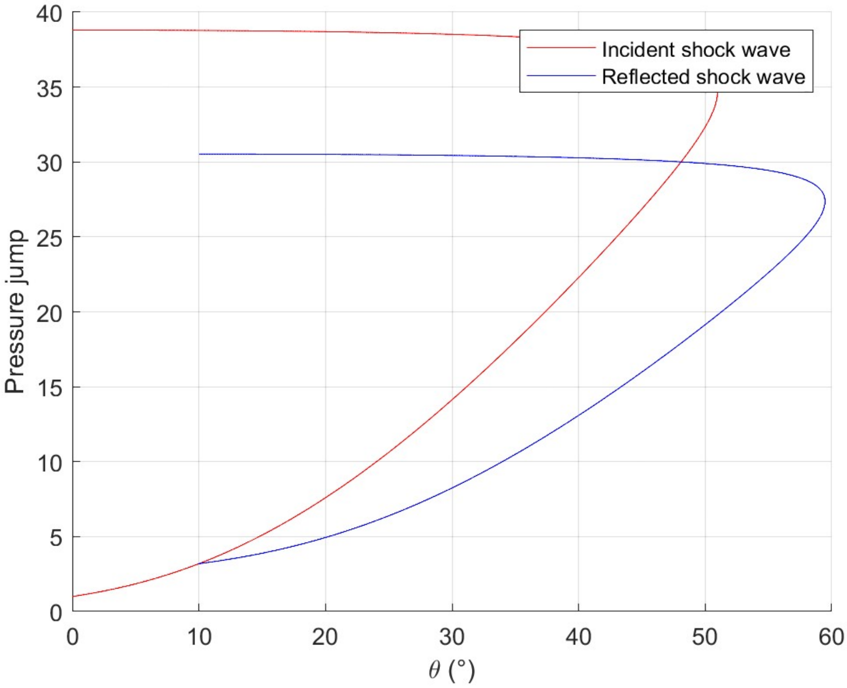

Figure 3.7: Shock polar

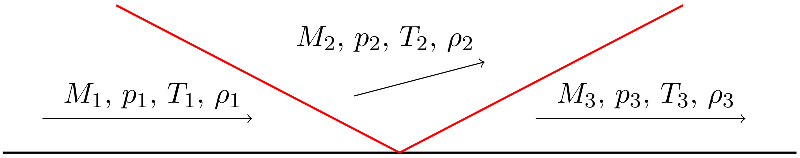

Figure 3.8: Regular reflection

M_2 and a higher θ_{max,M_2} are present, allowing to achieve the required deflection with a regular reflection.

3.3 Turbulence and mixing layer

In the mixing layer there is the interaction between the plume and the surrounding atmosphere due to the formation of vortices that transport the clean air within the plume, allowing the afterburning.
The mixing layer is characterized by high levels of turbulence, and its implementation has been done through the continuity equation (3.22), *Reynolds Averaged Navier-Stokes equations* (RANS) (3.23) and the energy equation (3.24). In particular, Reynolds decomposition has been used to obtain these equations, based on the idea of writing the instantenous flow variables, for example the velocity u, as the sum of a mean component ($\bar{u}$) and a fluctuating component (u'), thus

$$u(x,t) = \bar{u}(x) + u'(x,t)$$

At this point, the governing equations can be written as follows

$$\frac{\partial \bar{\rho}\bar{u}_j}{\partial x_j} = 0 \tag{3.22}$$

$$\frac{\partial(\bar{\rho}\bar{u}_i\bar{u}_j)}{\partial x_j} = -\frac{\partial \bar{p}}{\partial x_j} + \frac{\partial \overline{\tau_{ij}}}{\partial x_j} - \frac{\partial \bar{\rho}\overline{u_i'u_j'}}{\partial x_j} \tag{3.23}$$

$$\frac{\partial \bar{\rho}\bar{u}_j\bar{e}}{\partial x_j} = \frac{\partial}{\partial x_j}(k\frac{\partial \bar{T}}{\partial x_j}) + \overline{\tau_{ij}}\frac{\partial \bar{u}_i}{\partial x_j} - \frac{\partial}{\partial x_j}(\bar{\rho}\overline{u_j'e'}) \tag{3.24}$$

where $\overline{\tau_{ij}}$ is the mean viscous stress, defined as

$$\overline{\tau_{ij}} = \mu\left(\frac{\partial \bar{u}_i}{\partial x_j} + \frac{\partial \bar{u}_j}{\partial x_i}\right)$$

The RANS present also the term $\bar{\rho}\overline{u_i'u_j'}$, known as Reynolds stress, while the energy equations presents the term $\bar{\rho}\overline{u_j'e'}$, known as turbulent energy flux. They describe respectively the transportation of momentum and energy due to turbulent fluctuations, and require an additional model to close the RANS equations for solving.

Several turbulence models exist, each with its own characteristics. The chosen one is the **k-ε** model, thanks to its robustness and numerical stability for free jets away from a wall.

The model is based on the introduction of the turbulent kinetic energy k, defined as $k = \frac{1}{2}\overline{u_i'u_i'}$, and the turbulent dissipation rate ϵ, defined as $\epsilon = \nu\overline{\frac{\partial u_i'}{\partial x_j}\frac{\partial u_i'}{\partial x_j}}$, which represents the conversion rate of the turbulent kinetic energy into thermal energy. Both of these coefficients require an equation, which are

$$\frac{\partial \bar{\rho}\bar{u}_j k}{\partial x_j} = \frac{\partial}{\partial x_j}\left[\left(\mu + \frac{\mu_t}{\sigma_k}\right)\frac{\partial k}{\partial x_j}\right] + P_k - \bar{\rho}\epsilon \tag{3.25}$$

$$\frac{\partial \bar{\rho}\bar{u}_j \epsilon}{\partial x_j} = \frac{\partial}{\partial x_j}\left[\left(\mu + \frac{\mu_t}{\sigma_\epsilon}\right)\frac{\partial \epsilon}{\partial x_j}\right] + C_{1\epsilon}\frac{\epsilon}{k}P_k - C_{2\epsilon}\bar{\rho}\frac{\epsilon^2}{k} \tag{3.26}$$

where μ_t is the eddy viscosity, defined as

$$\mu_t = C_\mu\bar{\rho}\frac{k^2}{\epsilon} \tag{3.27}$$

and P_k is the production of turbulent kinetic energy, in the unclosed form given by

$$P_k = \bar{\rho}\overline{u_i'u_j'}\frac{\partial \bar{u}_i}{\partial x_j}$$

Empirical constants are also present, whose values are defined in the following table

C_μ	$C_{1\epsilon}$	$C_{2\epsilon}$	σ_k	σ_ϵ
0.09	1.44	1.92	1.0	1.3

Table 3.1: $k - \epsilon$ empirical constants

Thanks to the introduction of this model, Reynolds stress, turbulent energy flux and turbulent energy production terms can be rewritten through the Boussinesq approximation as follows

$$\bar{\rho}\overline{u_i'u_j'} \approx -\mu_t\left(\frac{\partial \bar{u}_i}{\partial x_j} + \frac{\partial \bar{u}_j}{\partial x_i}\right)$$

$$\bar{\rho}\overline{u_j'e'} \approx -\frac{\mu_t}{Pr_t}c_p\frac{\partial \bar{T}}{\partial x_j}$$

$$P_k = \mu_t\left(\frac{\partial \bar{u}_i}{\partial x_j} + \frac{\partial \bar{u}_j}{\partial x_i}\right)\left(\frac{\partial \bar{u}_i}{\partial x_j}\right) \tag{3.28}$$

where Pr_t is the turbulent Prandtl number, typically $Pr_t \approx 0.85 - 0.9$.

In this way the number of equations matches the number of unknowns, and the RANS system is closed and solvable through numerical methods.

3.3.1 Closing angle of the mixing layer

According to Section 2.5.1, the mixing layer is not negligible anymore starting from the transition region, from where it grows more and more. The implementation of this region and of the far field (Fig. 2.5) has been made through the following equation

$$\delta' = 0.14(1-r)\frac{(1+\sqrt{s})}{(1+r\sqrt{s})}\left(0.23 + 0.77e^{-3.5M_c^2}\right) \tag{3.29}$$

where $r = \frac{u_\infty}{u_{pc}}$, $s = \frac{\rho_\infty}{\rho_{pc}}$, $M_c = \frac{u_{pc}-u_\infty}{a_{pc}+a_\infty}$, $f_{pc} = 1.18 f_{exit} - 0.18 f_\infty$, with a speed of sound.
This equation has been validated by Poubeau (2015), and considers a linear development of the mixing layer with a constant closing angle that can be approximated as $\delta \approx \arctan\delta'$. In the region above the line defined by this angle, the mixing layer develops.
In addition to this, the equation leads to the fact that when the flow velocity at the exit of the nozzle matches the rocket velocity, $\delta = 0$, representing the fact that in this condition there is no mixing.

3.4 Chemical model

As introduced in Section 2.6, afterburning is an important phenomenon that must be taken into account in order to evaluate the atmospheric pollution caused by rocket launches. To do so, the formation and transportation along the plume of NO have been considered. This has been done in the mixing layer, where O_2 and N_2 are transported by vortices inside the plume to the boundary with the core where, due to the high temperatures, they react with the chemical species produced by the engine, forming NO through the Zeldovich mechanism.
The chemical model implemented must consider the fact that the NO production occurs at the boundary between the core and the mixing layer, and it has been described thanks to the species transport equation:

$$\nabla \cdot (\vec{v} C_j) = S_j \tag{3.30}$$

where $\vec{v}$ is the total flow velocity, C_j is the molar concentration of the species j, S_j is the production rate of the species, defined by the kinetic equation

$$S_\mathrm{j} = \frac{dC_\mathrm{j}}{dt} = k(T)[A]^a[B]^b[C]^c[D]^d \tag{3.31}$$

with the constant velocity $k(T)$ established by the Arrhenius equation presented in Section 2.3, with all the necessary parameters.
Regarding the concentrations of O_2 and N_2, these were considered using the NRLMSISE-00 model, which provides them as a function of altitude and date, while the concentrations of chemical species at the exit of the nozzle were considered through CEA. As can be noticed, the Zeldovich mechanism leads to the production of N and O, which are very reactive atoms, even at low temperature. This means that in the mixing layer association between these two species occurs, leading to an increase in the NO concentration in the plume. Obviously, the Arrhenius equation parameters change and are summarized in Table 3.2.

	A [m^3/mol/s]	E_a[kJ/mol]	n
$N + O \longrightarrow NO$	2×10^6	190	0
$NO \longrightarrow N + O$	1.3×10^6	160	0

Table 3.2: $N + O \rightleftharpoons NO$

3.5 Numerical methods

RANS equations form a nonlinear system that doesn't have an analytical solution, meaning that numerical methods must be used to compute the mixing layer flow field. The numerical solutions obtained will be affected by an error represented by the residuals, which indicate the deviation from the exact solution of an equation or a system of equations in a certain point of the domain, implying that a smaller residual generally indicates a more accurate solution.
In general, given a function *f*, its variation along a certain direction can be approximated through a finite difference method, which means calculating the f derivative as the variation of the function between two points separated by a small distance h. According to what previously introduced, it's possible to define

$$\frac{\partial f}{\partial x_i} \approx \frac{f(x_0+h)-f(x_0)}{h} \qquad \text{(forward difference)} \tag{3.32}$$

$$\frac{\partial f}{\partial x_i} \approx \frac{f(x_0)-f(x_0-h)}{h} \qquad \text{(backward difference)} \tag{3.33}$$

In order to solve an equations system with one of this methods, boundary conditions for every parameter are required. Another way to approximate a derivative is using a central finite difference method, based on the function values around the starting point, defining

$$\frac{\partial f}{\partial x_i} \approx \frac{f(x_0+h)-f(x_0-h)}{2h} \tag{3.34}$$

This method provides a second-order accurate solution, but it requires at least two initial values of the function.
The finite difference methods depend on the creation of a mesh in the flow field domain, that is creating a uniform grid of cells with dimensions dx and dy along the two directions where the equations are solved. In general, the smaller the value of dx and dy, the higher the accuracy but also the computational cost.
For example, the 2D continuity equation with central difference becomes

$$\frac{\partial \bar{\rho}\bar{u}}{\partial x} + \frac{\partial \bar{\rho}\bar{v}}{\partial y} = 0$$
$$\Downarrow$$
$$\frac{\bar{\rho}_{i+1}\bar{u}_{i+1} - \bar{\rho}_{i-1}\bar{u}_{i-1}}{2 \cdot dx} + \frac{\bar{\rho}_{i+1}\bar{v}_{i+1} - \bar{\rho}_{i-1}\bar{v}_{i-1}}{2 \cdot dy} = 0$$

Applying a finite difference method is really important, since it allows to transform a differential equations problem, often a strongly nonlinear system, into a system of equations that can be solved more easily.
The equations obtained by the application of a finite difference method to RANS, even if easier than the original ones, are coupled and strongly nonlinear, forming a really complicated system denoted $F(x)$. In order to solve it, the generic method of imposing

$$F(x) = 0$$

is not the best option, since finding for every point a solution vector that satisfies the relation is really difficult and may lead to numerical instabilities.
To avoid this, the solution method chosen is the nonlinear least squares method, which consists in minimizing the local residual error between the exact solution and the approximated solution, solving

$$\min \|F(x)\|^2 \tag{3.35}$$

In addition to the RANS, the equations (3.14) and (3.21) are transcendental for M_2 and β, meaning that they cannot be solved analytically using algebraic methods. In this case, an iterative numerical technique is required, such as the so-called Newton-Raphson method. This method is based on the idea of finding the roots of an equation through successive approximations until a sufficiently precise value is reached. This implies that the Newton-Raphson method requires an initial guess for the root.
The method solves the following equation for a given function f

$$x_{n+1} = x_n - \frac{f(x_n)}{f'(x_n)} \tag{3.36}$$

and requires knowledge of the exact derivative f'. If this is not known, the Newton-Raphson method can be approximated using the secant method, writing the derivative as

$$f'(x_n) \approx \frac{f(x_n) - f(x_{n-1})}{x_n - x_{n-1}} \tag{3.37}$$

requiring in this way two initial values x_0 and x_1.
The secant method has been used to evaluate the Mach number at the end of the expansion between the nozzle exit and the reflection point, where the static pressure reaches the atmospheric value. In this way, the $\frac{p_2}{p_1}$ ratio is known and allows the calculation of M_2, assuming $M_1 = M_\mathrm{e}$. In addition, it has been used to evaluate the wave angle of the reflected shock β after the calculation of the deflection angle θ from the shock polar, for the Mach reflection regime.

3.6 Model implementation

The implementation of the model so far illustrated has been done in MATLAB, where a main and a certain number of functions are used. The main contains:

- Plume composition: mass fraction of O, OH, O_2, H for NO production and mass fraction of the species with $w_\mathrm{j} > 10^{-5}$ for transport properties. Obtained through CEA calculations, they are required to compute the NO production and transport properties using Eq. 3.8 and Eq. 3.9.
- Thermodynamic parameters: such as Mach number, temperature, pressure, density, γ, used as initial conditions. Also these are calculated thanks to CEA.
- Sutherland coefficients: for the chemical species, for calculating μ_mix.
- Trajectory: velocity, latitude, longitude, altitude.
- Number of cells: the computational domain, that is the studied volume, is divided into small elements with defined dimensions, the cells, where the equations are solved. This process is called discretization.

The main goal is studying how the emissions change along the trajectory and which parameter at the nozzle exit more affects them. So, once the different points along the trajectory are set and one parameter has been chosen as variable, NO formation is estimated for every altitude and for every value of the variable. In the main, the calculation for the plume structure and the emissions are not computed: here, a part from the values already introduced, there is only a function call to the primary function, which in turn presents 3 other function calls. So, in total there are 4 functions, summarized as follows:

1. `underexpanded`: computes the entire plume, simulating the flow behavior for every cell of the domain implementing all the equations of the model.

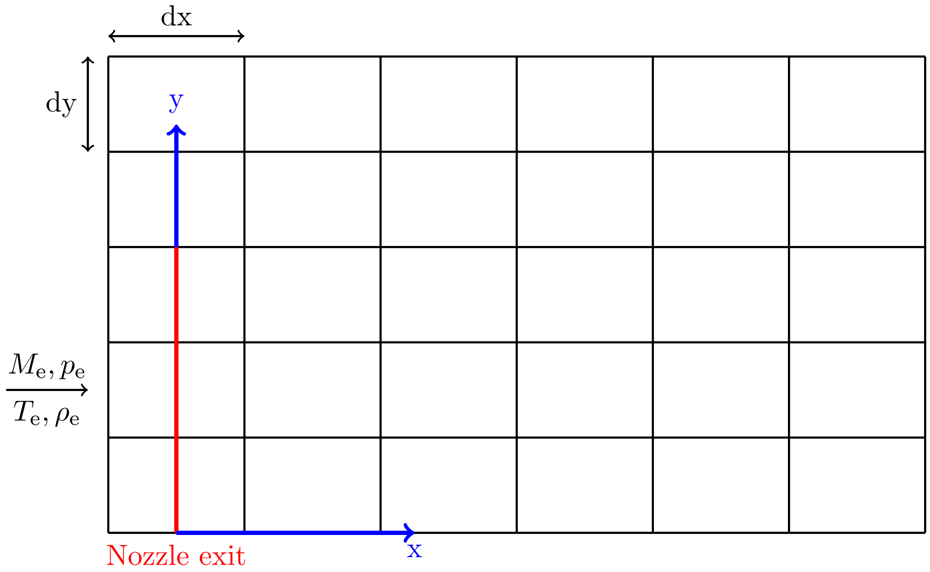

Figure 3.9: Structured mesh with the reference system of half the computational domain

2. `RANS`: solves the RANS equations numerically through the nonlinear least squares method, implemented by the MATLAB function `lsqnonlin`, which besides allows to monitor the residual values. The equations are rewritten thanks to the finite difference method.
3. `shock-polar`: calculates the deflection angles of the reflected shock wave for the Mach reflection regime.
4. `transport-properties`: based on the plume composition, it is used to determine μ_{mix} and k_{mix}, necessary for solving RANS.

The first thing to implement it's the discretization of the 2D computational domain. Considering that higher is the number of cells chosen, higher is the computational cost, the spatial step along the x direction dx, that is the dimension of the cells in that direction, is calculated as

$$dx = \frac{L_{\text{plume}}}{N_x - 1} \tag{3.38}$$

where N_x is the number of cells chosen and L_{plume} is the length of the plume, arbitrarily assumed equals to a certain value that changes if the mixing layer closes further downstream the supposed length.

Then the relation $dy = 0.5 \cdot dx$ is established as a good compromise between accuracy and computational cost.

Once this is done, a $x-y$ coordinate system must be implemented, with x downstream the nozzle, y parallel to it. This allows the definition of the position of the cells, both the edges and the centers, leading to the structured mesh shown in Fig. 3.9, a mesh with regularly disposed nodes. In addition to this, since a symmetric plume is considered, just half of the computational domain is considered to reduce the computational cost.

The next step, after defining the different quantities of the main, it's calculating the opening angle of the plume. The NRLMSISE-00 model provides the atmospheric temperature and density based on altitude, latitude, longitude and date. Thanks to ρ_{amb} and T_{amb}, it's possible to calculate p_{amb}, which is useful for estimating the opening angle of the plume following Eq. (3.12). This is possible because the ratio $p_2/p_1 = p_{\text{amb}}/p_e$ is defined and helps calculating M_r with Eq. 3.17 and, later, the fan opening angle with Eq. (3.11). Through this the slipline can be defined and the plume approximated with conical expansion until its pressure reaches the ambient value. Beyond this point, the mixing layer starts, the plume boundary is approximated as parallel to the axis and develops downstream until the mixing layer closes.

Afterwards, the closing angle of the mixing layer, the expansion at the nozzle exit (that is the distribution of Mach number, temperature, pressure and density between the nozzle exit and the reflection point) and the incident oblique shock wave are introduced simply implementing the equations (3.29), (3.13)-(3.15), (3.16)-(3.19). The incident shock wave β is calculated from (3.17), considering the pressure jump as a percentage of a normal shock wave that depends on the altitude. β is then assumed to be constant for the entire shock wave.

At this point, the reflection regime has to be determined. This is done in the following manner:

1. For simplicity, a regular reflection regime is assumed when the incident shock wave is calculated.
2. $\theta_{\max,M_2}$ is calculated for every cell after the incident shock, determining the values of θ for the post-shock Mach number, for every β from θ_{M} to 90° and deriving the maximum value from this.
3. θ_{M_2} is derived from Eq. 3.21 and then compared with $\theta_{\max,M_2}$, for every cell.
4. If there is a cell where the Mach reflection condition $\theta_{M_2} > \theta_{\max,M_2}$ is respected, then from that cell the Mach disc develops and the normal shock waves relations are implemented for the post-shock parameters. Otherwise, the assumption of regular reflection regime is valid.

If the condition of Mach reflection is respected, the reflected shock wave must be defined, which means that θ and β are required. These are established in the function `shock-polar`. It draws the $p-\theta$ curves for the before and post incident shock wave Mach number using the $\theta-\beta-M$ relation (Eq. (3.21)) and the pressure jump across the shock wave (Eq. (3.17)). Then, it checks for an intersection between the two curves, which represents θ of the reflected shock wave. Again, using the $\theta-\beta-M$ relation, the β is obtained, defining in this way the reflected shock geometry.

If the Mach reflection condition is not respected, the flow is in regular reflection, then the condition $\theta_1 + \theta_2 = 0$ is implemented for every cell, and β is calculated through Eq. (3.21). In this case, the geometry is also defined and the shock wave is calculated. Independently of the reflection regime, the reflected shock wave β is considered to be constant, just like the one for the incident shock wave.

Now, the entire inviscid core has been developed; therefore, the mixing layer follows. Based on its already obtained geometry, the `RANS` function is called. Here, there is the approximated system of the RANS equations solved through the `lsqnonlin` MATLAB function. This leads to the calculation of Mach number, x- and y-velocity, pressure, temperature, density, dissipation rate, turbulent kinetic energy and turbulent viscosity, cell by cell, till the point where the mixing layer closes.

In the end, the NO production must be estimated. First of all, the Arrhenius equations (2.1) for the constant velocities for the Zeldovich mechanism are defined, implementing in MATLAB Tab. 2.3 and 2.4. Then, the convective transport of the atmospheric N_2 and O_2 within the plume and the distribution of O, OH, O_2, H within the inviscid core are carried out thanks to the transport equation (3.30). As the other differential equations, it has been approximated using a finite difference method in order to solve it. Then, the kinetic equation 3.31 at the boundary between the inviscid core and the mixing layer is implemented, which simulates the initial NO mass produced by the interaction between the mixing layer and the hot inviscid core. NO is so transported downstream and the reaction between the radicals N and O changes the estimated pollutant. This reaction is applied in the same way the Zeldovich mechanism is applied. In particular, the kinetic equation is written for every chemical species involved in the reactions,

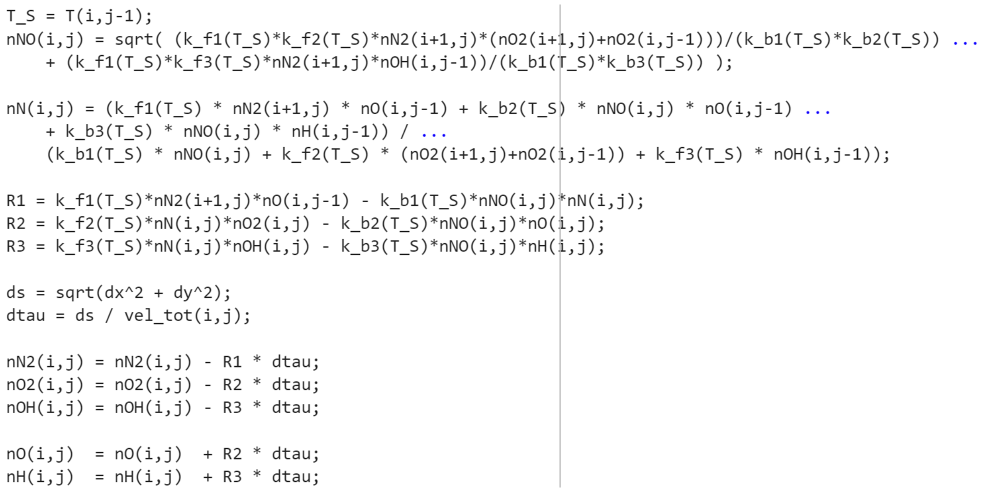

```
T_S = T(i,j-1);
nNO(i,j) = sqrt( (k_f1(T_S)*k_f2(T_S)*nN2(i+1,j)*(nO2(i+1,j)+nO2(i,j-1)))/(k_b1(T_S)*k_b2(T_S)) ...
    + (k_f1(T_S)*k_f3(T_S)*nN2(i+1,j)*nOH(i,j-1))/(k_b1(T_S)*k_b3(T_S)) );

nN(i,j) = (k_f1(T_S) * nN2(i+1,j) * nO(i,j-1) + k_b2(T_S) * nNO(i,j) * nO(i,j-1) ...
    + k_b3(T_S) * nNO(i,j) * nH(i,j-1)) / ...
    (k_b1(T_S) * nNO(i,j) + k_f2(T_S) * (nO2(i+1,j)+nO2(i,j-1)) + k_f3(T_S) * nOH(i,j-1));

R1 = k_f1(T_S)*nN2(i+1,j)*nO(i,j-1) - k_b1(T_S)*nNO(i,j)*nN(i,j);
R2 = k_f2(T_S)*nN(i,j)*nO2(i,j) - k_b2(T_S)*nNO(i,j)*nO(i,j);
R3 = k_f3(T_S)*nN(i,j)*nOH(i,j) - k_b3(T_S)*nNO(i,j)*nH(i,j);

ds = sqrt(dx^2 + dy^2);
dtau = ds / vel_tot(i,j);

nN2(i,j) = nN2(i,j) - R1 * dtau;
nO2(i,j) = nO2(i,j) - R2 * dtau;
nOH(i,j) = nOH(i,j) - R3 * dtau;

nO(i,j)  = nO(i,j)  + R2 * dtau;
nH(i,j)  = nH(i,j)  + R3 * dtau;
```

Figure 3.10: Code for the Zeldovich mechanism

rewriting the term $S_\mathrm{j} = dC_\mathrm{j}/dt$ as

$$S_\mathrm{j} = dC_\mathrm{j}\frac{\sqrt{u^2 + v^2}}{\sqrt{dx^2 + dy^2}}$$

considering that the flow is no longer 1D, but 2D.
Assuming now that the concentration of N slightly changes, due to the low concentration of this species compared with others, it's possible to simplify the NO kinetic equation, avoiding a system of differential chemical equations difficult to solve. Subsequently, the production or consumption of the other chemical species can be estimated. The implementation of this is presented in Fig. 3.10.
Given its implementation and assumptions, the model can be classified as a reduced-order model, with a significantly lower computational cost compared to standard CFD codes.

4 Results

The model described in Chapter 3 makes it possible to estimate the NO emissions of rockets at different altitudes, to understand how they evolve along the trajectory, and for different engine architectures, comparing the environmental impact of different launch systems.
This Chapter first analyzes the Mach number, temperature and pressure distribution within the plume. Then, for a general architecture, the emissions along the trajectory to the orbit are evaluated, the NO distribution studied and the difference between a Frozen and an Equilibrium composition in the nozzle checked, looking for the worst case scenario. In the end, the effect of atmospheric fluctuations and notable engines are studied.
The analysis requires the calculation of the parameters at the nozzle exit as boundary condition. As previously mentioned, these are obtained using CEA, which requires some inputs, in particular the propellants, the expansion ratio, the chamber pressure and the mixture ratio, respectively RP-1 and LOX, $\epsilon = 16$, $p_c = 96$ bar, MR = 2.3. With these inputs, CEA produces the following parameters for flow at the nozzle exit

Ma	p_e [bar]	ρ_e [kg/m^3]	T_e [K]	γ	M [1/n]
3.511	0.68443	0.10705	1828.18	1.2148	23.774

4.1 Variables distribution

The distribution of Mach number, temperature and pressure are important, since they are an indicator of how the plume evolves in the atmosphere, how intense the different phenomenon are and their effects on the plume itself.

4.1.1 Mach reflection regime

The Mach number distribution can be seen in Fig. 4.1. The inviscid core and mixing layer are clearly visible. Starting from the nozzle exit, the shock wave structure can be observed, with the reflected shock and the Mach disc that decrease the Mach number. Further downstream, the mixing layer develops. Here, two facts can be noticed. The first one is that, for most of it, the Mach number is almost constant due to the fact that the mixing is weaker and weaker getting closer to the centerline, leading to a low exchange of momentum and energy, meaning that velocity and temperature change slightly within this part of the region. The second fact is that, close to the border with the atmosphere, the mixing is effective and the momentum and energy exchanges are stronger, leading to a decrease of the velocity and of the temperature, which adapts to the external one. The second effect is stronger than the first, leading to an increase of the Mach number. This is the region where vortices develop, which are very important since they trigger the mixing between the atmosphere and the plume. These are not visible in the graph since it represents only the magnitude of the Mach number and not the direction, although the energetic effects are taken into account and play a key role.

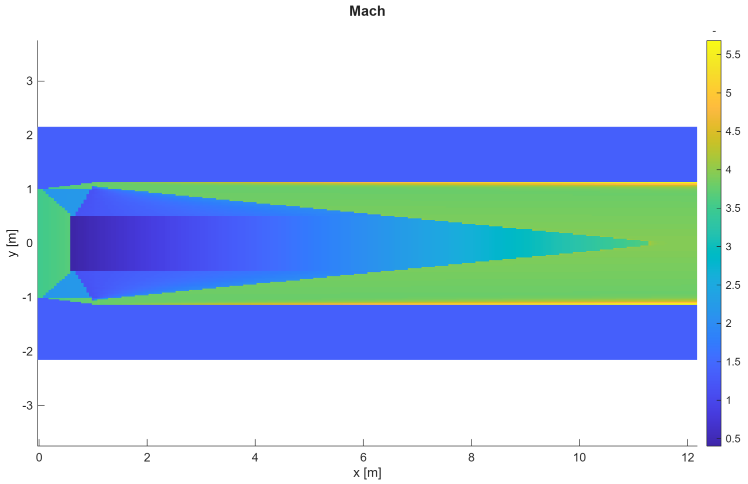

Figure 4.1: Mach distribution in Mach reflection regime

Now, let's take a closer look to the inviscid core, referring to Fig. 4.2. The Mach reflection structure can be easily noticed, with the incident shock, the reflected shock and the Mach disc that meet in the triple point. The flow post the two oblique shock waves keeps being supersonic, meaning that both of them are weak shock waves, while the post Mach disc flow is subsonic, as predictable for a normal shock wave.

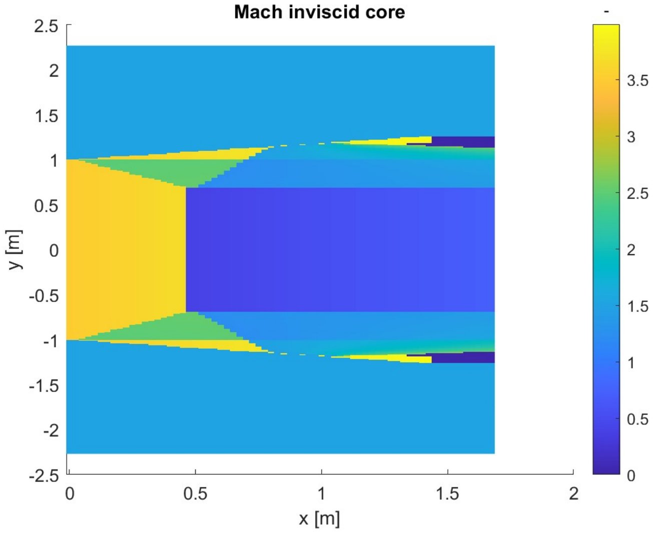

Figure 4.2: Inviscid core in Mach reflection regime

At this point, the temperature distribution can be analyzed (Fig. 4.3). The effect of the presence of the shock waves is clearly visible by Fig. 4.4 representing the inviscid core, that suggest high temperatures within this region. These are caused in particular by the Mach disc, since normal shock waves cause the highest temperature jumps. It's also visible the temperature drop after the different shock waves, caused by the expansion of the gas. Taking a closer look to the mixing layer, as in Fig. 4.5, what previously discussed about the temperature next to the boundary with the atmosphere can be noticed, with the drop caused by the effective mixing.

Eventually, the pressure is examined. Analyzing the inviscid core from Fig. 4.6, one of the main characteristic of the Mach reflection is evident, which is the pressure after the shock wave. This, as explained in Section 3.2.3, must be the same downstream the Mach disc and the reflected

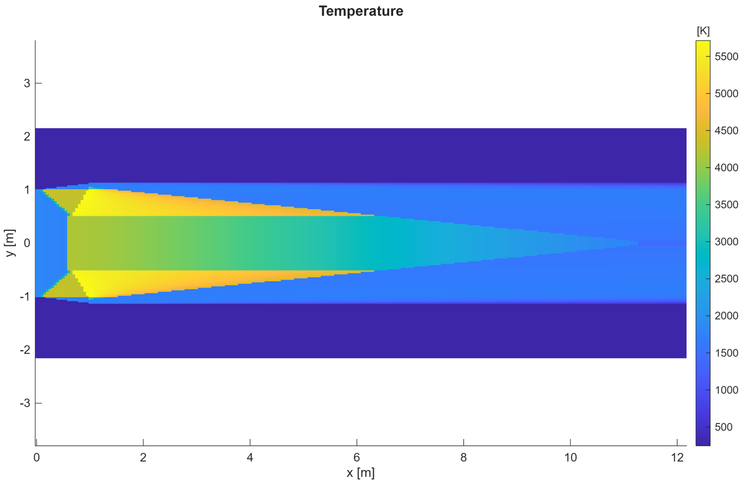

Figure 4.3: Temperature distribution in Mach reflection regime

shock wave in order to avoid pressure gradients that would create vertical velocity components, while the other parameters can be, and effectively are, different.

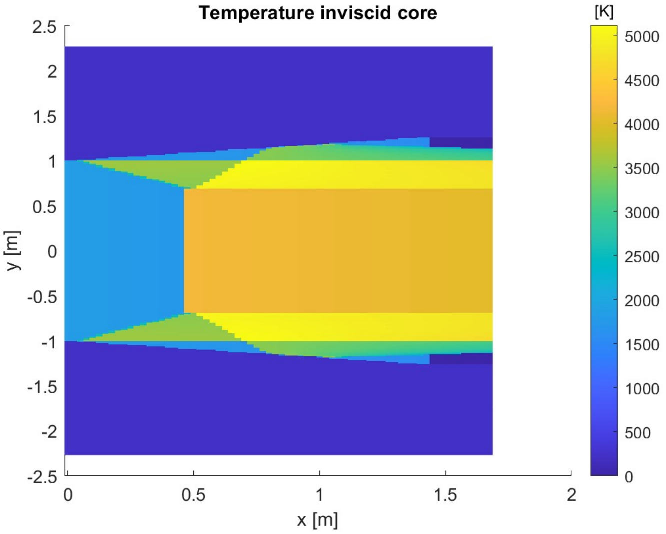

Figure 4.4: Temperature distribution in the inviscid core for Mach reflection regime

4.1.2 Regular reflection regime

As previously mentioned, the regular reflection regime is characterized by a colder plume than the Mach reflection regime due to the shock wave structure that doesn't present the Mach disc, but just the incident shock wave and the reflected shock wave which realign the flow. This is relevant for the analysis, since on this all the differences with Mach reflection in the variables distribution can be justified.

As regard the Mach distribution in Fig. 4.7, different things can be noticed. First of all, the point where the mixing layer closes is definitely further downstream than the same in Mach reflection. This is because regular reflection occurs at high altitude, where the rocket velocity is high and the angle of the mixing layer decreases, with reference to Eq. (3.29). The second thing is the fact that the minimum value of the Mach number, again compared with Mach reflection, is definitely

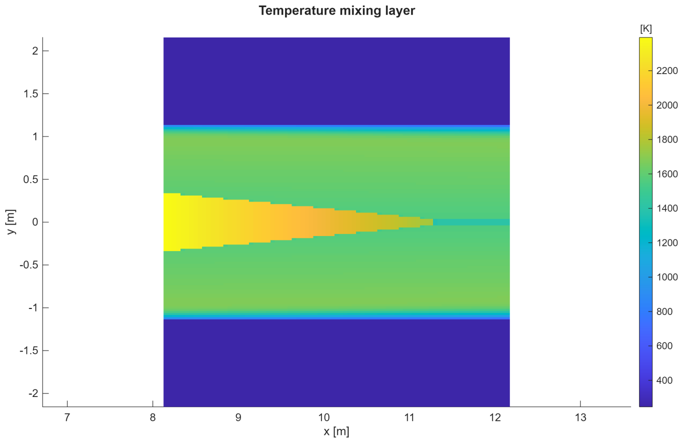

Figure 4.5: Temperature distribution in the mixing layer for Mach reflection regime

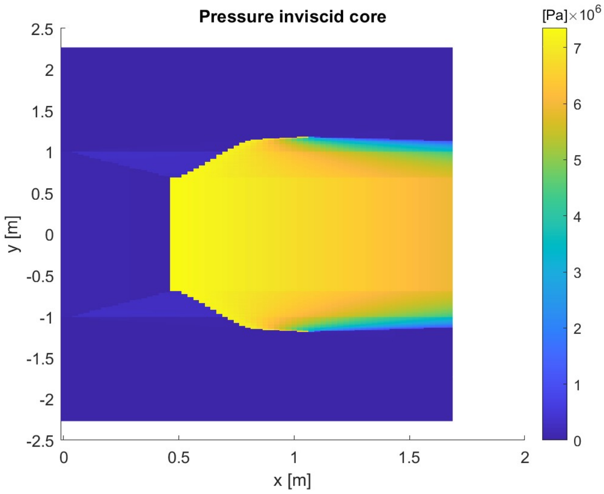

Figure 4.6: Pressure distribution in the inviscid core for Mach reflection regime

higher in the inviscid core because of the absence of the Mach disc, which always causes a subsonic flow downstream. This is valid also in the rest of the mixing layer, where the values of Mach number are increased for the low temperature. The last thing is the Mach in the boundary region between the plume and the atmosphere. Here, as in Mach reflection, the value is higher than the rest of the mixing layer, and in this regime even higher. This is because of a colder atmosphere, since the high altitude, and a colder plume, for the inviscid core structure. The exchange of momentum and energy is here efficient, and these conditions lead to a lower temperature in the region and so a higher Mach number.
Taking now a closer look to the inviscid core in Fig. 4.8, the reflection structure is visible, with the reflection at the reflection point. It's also clear the expansion after the nozzle exit, that makes the flow faster and the shock wave more intense in the centerline, even though the Mach number is here higher compared with the rest of the shock wave.
The analysis of the temperature distribution can be done now. Referring to Fig. 4.9, noticeable is the fact previously mentioned that the plume is colder if compared with the Mach reflection, with temperatures in the mixing layer that can be up to half of it according to the legend. Also, unlike before where the highest temperature could be found after the Mach disc, in the central part of the inviscid core, now the highest temperatures can be found in the centerline, due to the fact that here the shock waves are really close and so the flow doesn't cool down before crossing

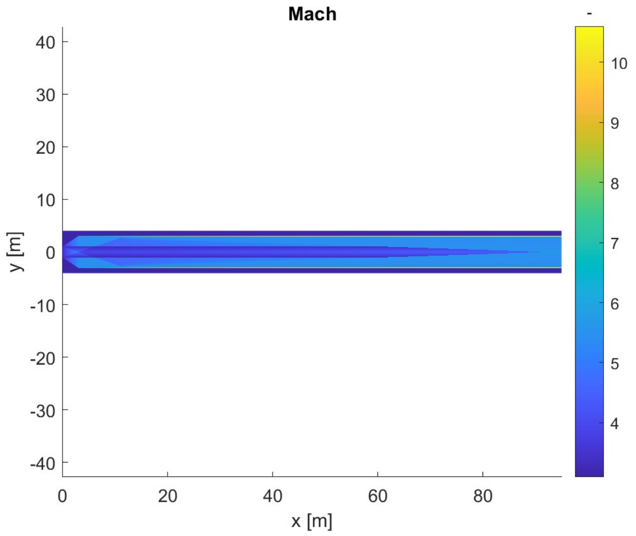

Figure 4.7: Mach distribution in regular reflection regime

the second one; and in correspondence of the nozzle lips, since the flow is already hot and crosses the shock wave almost immediately, making it the hottest part of the plume.

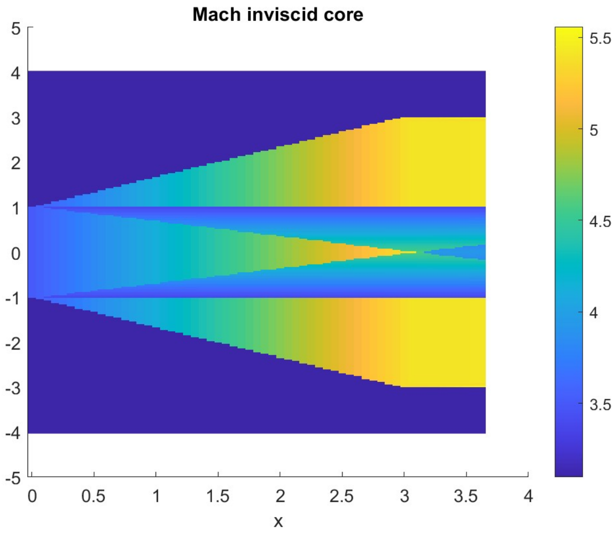

Figure 4.8: Mach distribution in the inviscid core for regular reflection regime

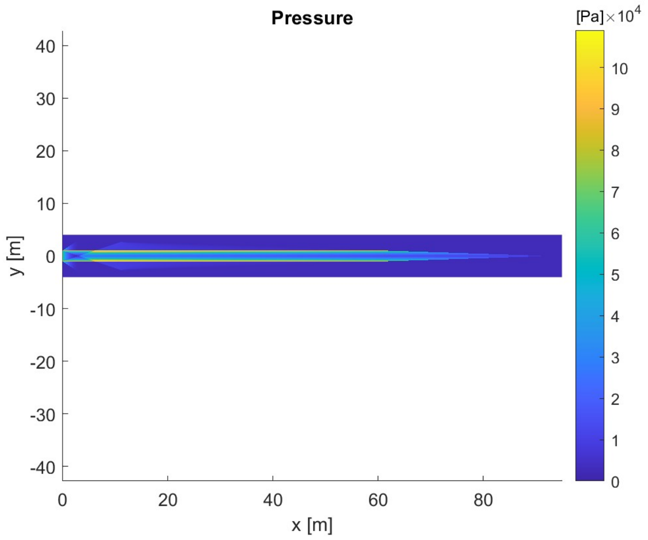

Figure 4.10: Pressure distribution for regular reflection regime

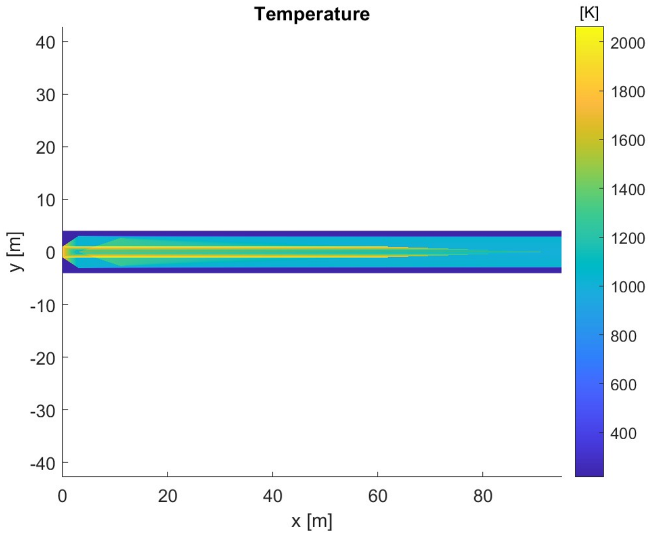

Figure 4.9: Temperature distribution in regular reflection regime

In the end, the pressure distribution is analyzed (Fig. 4.10). The behavior in the inviscid core is basically the same as the temperature, with the maximum values in the centerline and in correspondence of the nozzle lips, while in the mixing layer the behavior is the same as in the Mach reflection regime, with the pressure that adapts to the ambient conditions to avoid continuous reshape of the plume.

4.1.3 Plume opening angle and mixing layer angle

By observing Fig. 4.11, it is evident that with increasing altitude the opening angle of the plume increases. This is a direct consequence of Eq. 3.12 and Eq. 3.14, since higher the altitude is, lower p_{amb} is and so M_{r} increases. Therefore, the term $\nu(M_{\mathrm{r}}) = \nu(M_2)$ is bigger while $\nu(M_{\mathrm{e}}) = \nu(M_1)$ remains constant, depending only on the nozzle exit conditions (Eq. 3.11). This means that the opening angle θ grows.

As regards the mixing layer closing angle, Fig. 4.12 shows that with increasing altitude, the closing angle decreases as stated by Eq. 3.29. In fact, with increasing altitude the velocity of the rocket increases and tend to be more similar and more similar to the nozzle exit velocity, causing smaller angles to form.

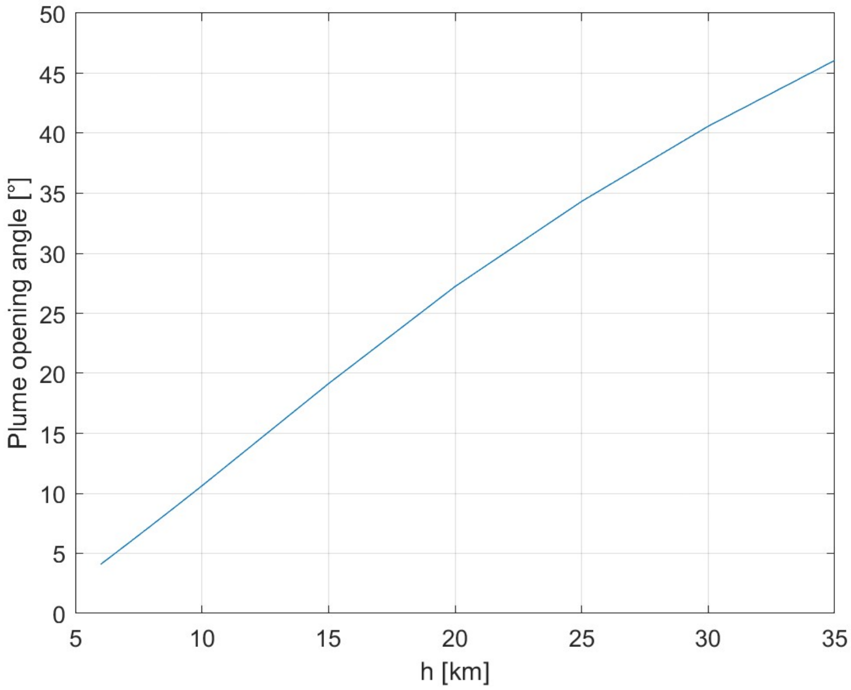

Figure 4.11: Changing of the plume opening angle with altitude

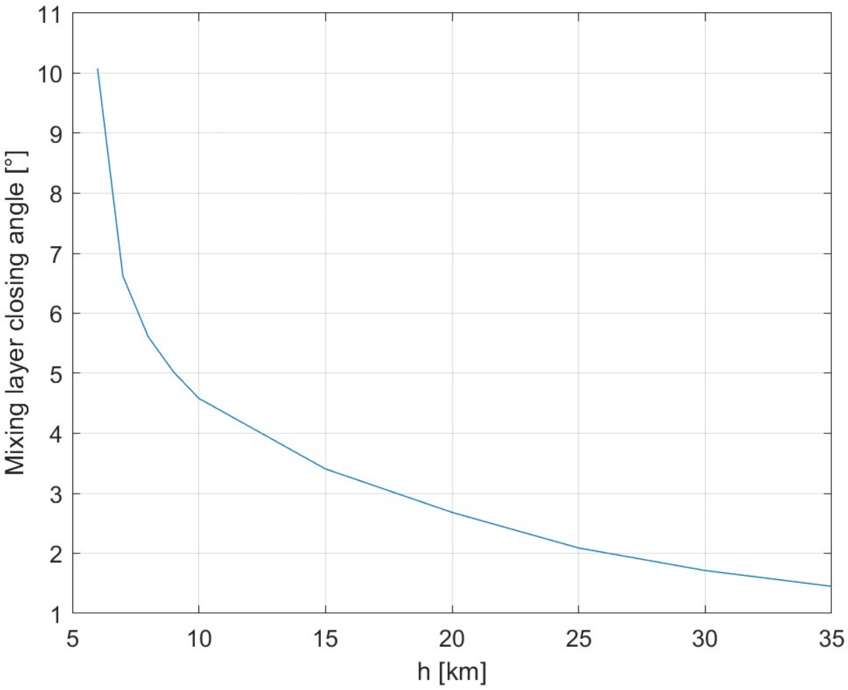

Figure 4.12: Changing of the mixing layer closing angle with altitude

4.2 NO distribution and along the trajectory

Firstly, the study about the differences in the NO distribution in the different regimes can be conducted.
As a consequence of the different plume structures that cause a different temperatures distribution, the production is more triggered in the Mach reflection regime. In particular, following Fig. 4.13, it can be noticed that the maximum production is located where the mixing layer interacts with the flow that has crossed the Mach disc and it's therefore at significant high temperature. According to Fig. 4.14, the higher production is placed, as predictable, in line with the nozzle lips, where the plume is hotter in this configuration.
Observing the legends of Fig. 4.13 and Fig. 4.14, it appears that there is a difference of two orders of magnitude in the molar concentration of the species. The high temperatures of the first configuration results in higher values of $k(T)$ (Eq. 2.1 and Fig. 2.1) and so higher NO production, while in the second configuration $k(T)$ assume lower values, resulting in a lower production.
After this, the variation of the emissions along the trajectory must be studied. According to what discussed in Section 2.6, the NO should decrease with the altitude because of the lower availability of N_2 and O_2 in the atmosphere and a faster rocket. And this behavior has been well captured by the implemented model, as shown in Fig. 4.15.
Since NO can vary by several orders of magnitude with altitude, it can be useful using a logarithmic plot instead of a linear one, which generates the results in Fig. 4.16 where it's possible to notice a sudden drop of NO mass between 20 and 25 km. This can easily be explained by the transition from Mach reflection to regular reflection in that altitude range.

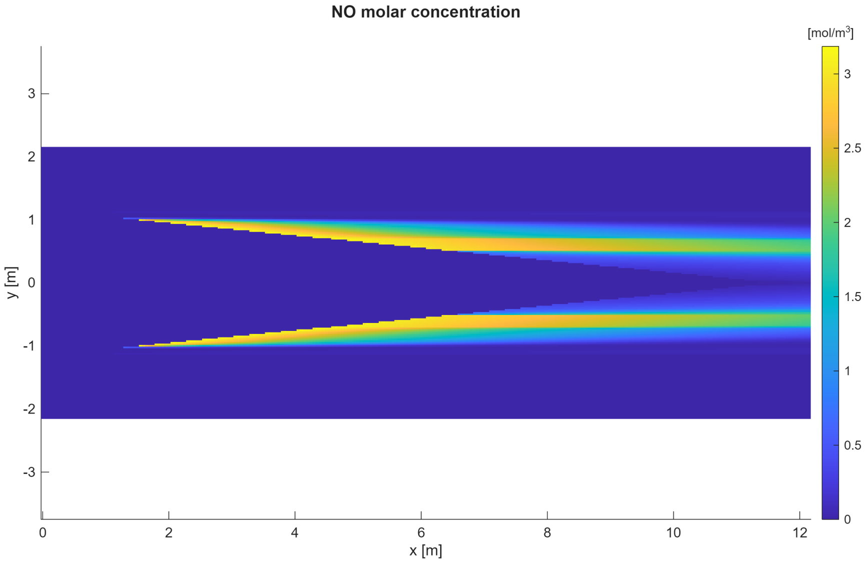

Figure 4.13: NO distribution for Mach reflection regime

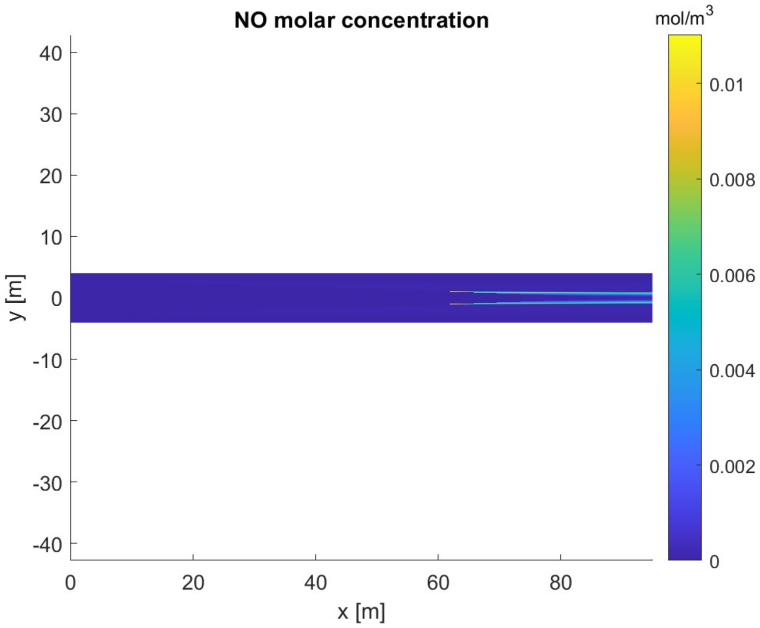

Figure 4.14: NO distribution for regular reflection regime

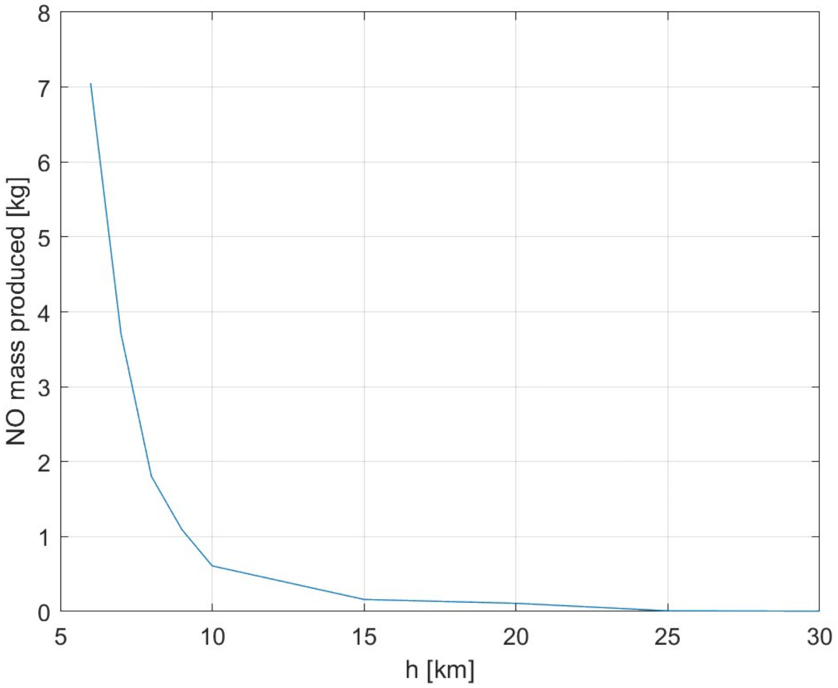

Figure 4.15: Variation of NO emissions with altitude

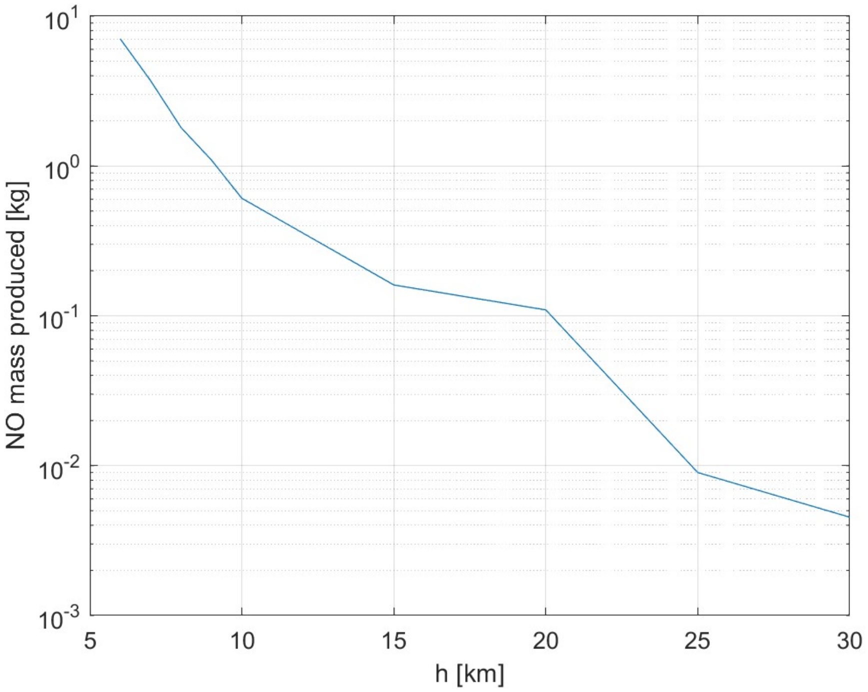

Figure 4.16: Logarithmic variation of NO emissions with altitude

4.3 Equilibrium vs. Frozen

In the CEA output file, the output parameters are present twice. This occurs because CEA performs two different analyses with two different models for the nozzle: equilibrium model and frozen model. The first refers to a nozzle where the gas composition adjusts at each point to maintain chemical equilibrium; the second refers to a gas whose composition remains fixed along the nozzle. This distinction is important, since the model used strongly influences the estimated NO produced. This happens because in the combustion chamber, the combustion leads to the dissociation of the chemical species. In the case of an equilibrium flow, these species can partially recombine in the divergent section, releasing energy that makes the flow faster and hotter. As a result, the exit temperature is higher than in the frozen case, leading to a greater NO production. Therefore, the equilibrium flow can be often considered as a worst-case scenario, and from now on it will be the considered approach.
What previously discussed can be observed in Fig. 4.17 The difference between the two models appears to be clear, in particular if the percentage variation is calculated with reference to the equilibrium emissions and plotted along the trajectory, as in the following figure. It can be noticed the fact that the mass produced is definitely higher with the equilibrium model, reaching almost a double amount at 20 km.

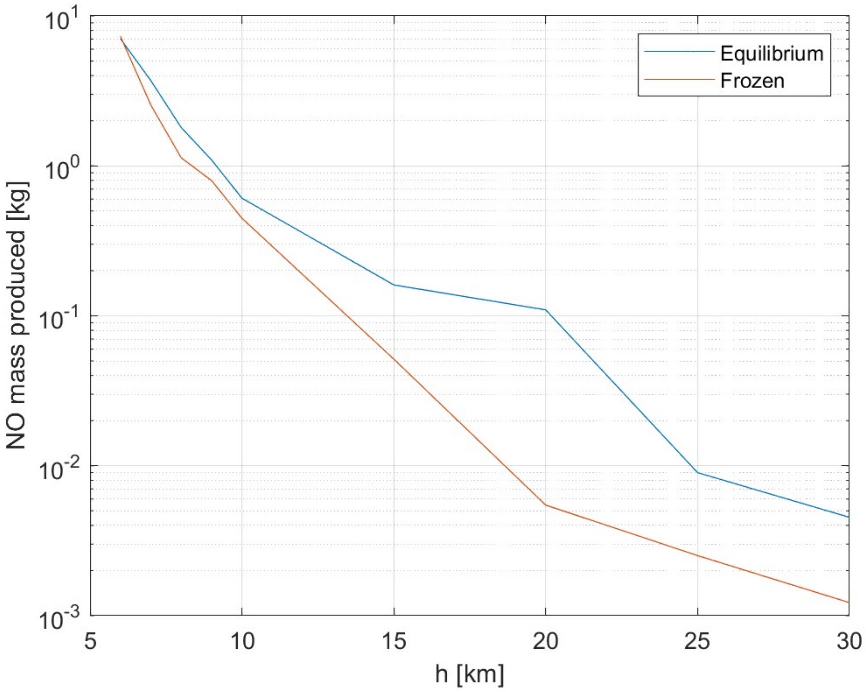

Figure 4.17: Comparison between equilibrium and frozen flow

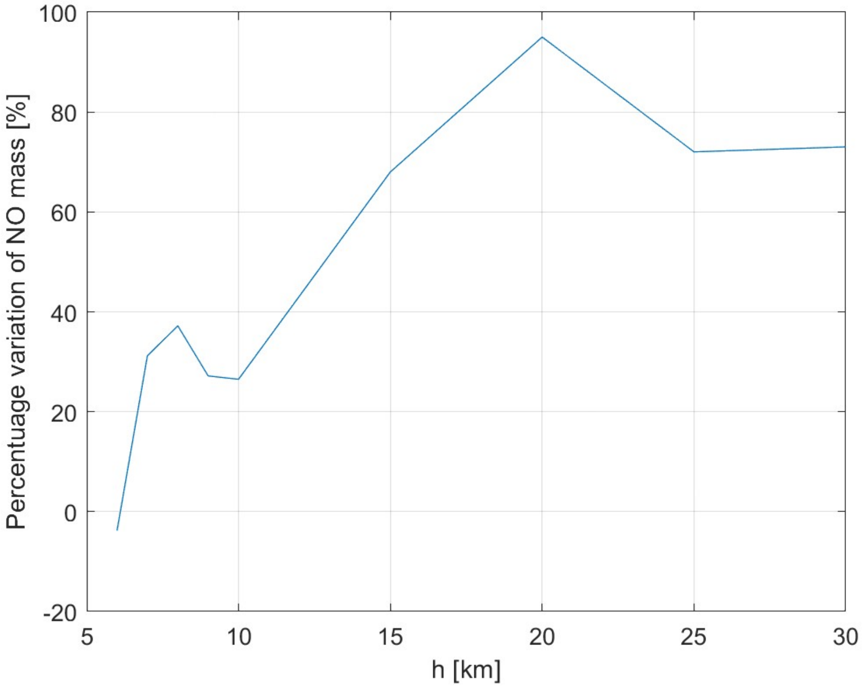

Figure 4.18: Percentage variation of emissions between Equilibrium and Frozen models

4.4 Emissions variation with the exit parameters

At this point, the emissions variation with temperature, pressure, Mach number at the nozzle exit and the nozzle diameter are studied.

4.4.1 Temperature

The figure 4.19 shows the behavior of the emissions along the trajectory for different temperatures at the nozzle exit, from 6 km to 10 km, 15 km, 20 km and 25 km, and from 1000 K to 4500 K. The temperature profile for every altitude is basically similar, with an initial increase of the production with higher temperatures, reaching a local maximum followed by a decrease till a local minimum. After that, the production starts rising again, probably approaching an asymptote at higher temperatures. Another noticeable fact is that the position of both the local maximum and the minimum change with altitude, shifting to higher temperature.
An explanation for this profiles comes from Eq. (3.13). With fixed $M_1 = M_\mathrm{e}$ and $M_2 = M_\mathrm{r}$, an increase of $T_1 = T_\mathrm{e}$ implies an increase of $T_2 = T_\mathrm{r}$. This means that, being M_r only dependent on p_amb and p_e, and not on T_e, at fixed altitude the pre-shock Mach number and the shock wave's β are constant and therefore, from Eq. (3.18), the temperature jump does not change. This leads to a higher post-shock temperature, a hotter plume and a higher NO production.
However, a local minimum that shifts to the right as the altitude rises can be observed, and this seems to go against what previously explained. As explained in Section 4.4, NO is produced both through the Zeldovich mechanism and the reaction between the radicals O and N. When T_e rises, the dissociation of N_2 and O_2 in the plume increases, meaning that the availability of these chemical species for the Zeldovich mechanism is minor. At the same time, the concentration of radicals is still insufficient for the $\mathrm{N} + \mathrm{O} \longrightarrow \mathrm{NO}$ reaction to significantly increase NO production, due to the high dissociation energy requested. These combined effects result in a decrease in NO

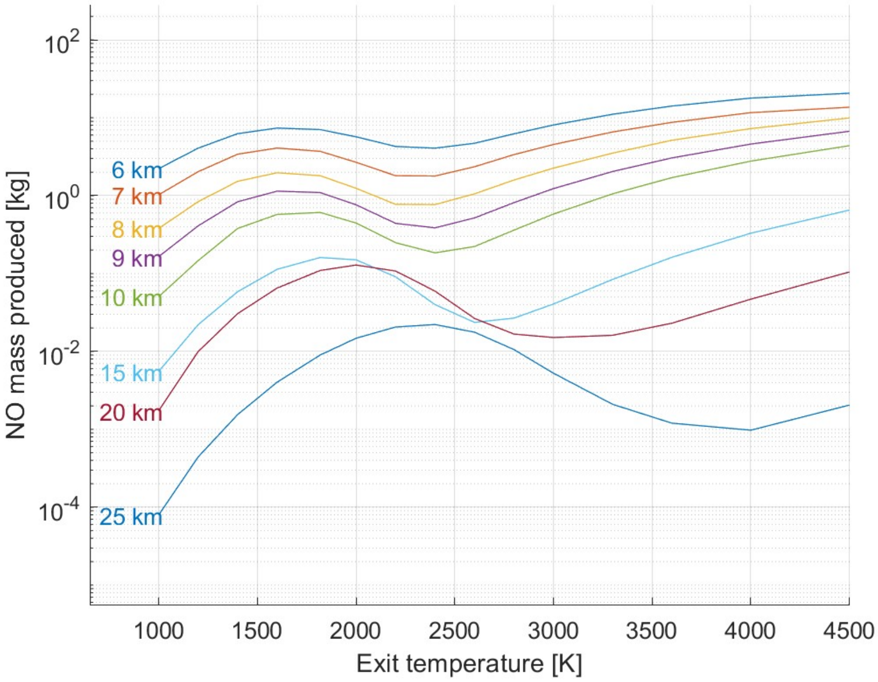

Figure 4.19: NO emissions profiles at different altitudes for different T_e

production. At a certain point, further increase in T_e results in a higher production: there is a transition, represented by the minimum, between the Zeldovich mechanism and the radicals reaction as the dominant reaction.
The shifting of the minimum as altitude rises can be then explained as follows: since at higher altitude N_2 and O_2 are less available, higher temperatures are required to produce the sufficient amount of radicals so that the reaction is able to initiate.

4.4.2 Pressure

Analyzing Fig. 4.20, the pressure profiles for different exit pressure and altitudes are plotted, for pressure from 0.5 bar to 3 bar and the same altitudes as the temperature study. The evolution of the emissions with the exit pressure depends on the altitude: for lower altitudes, the profiles present an increasing trend with increasing conditions, until they become almost constant; at 15 km, the profiles tend to follow the same trend, but suddenly a drop in the emissions occurs, and from there on, the emissions change slightly. At 20 km and 25 km, the drop and the increase observed at lower altitudes are not present, while the emissions variation is small.
The initial increase at lower altitude can be explained as follows: when the exit pressure increases, at fixed altitude and M_e, then according to Eq. (3.14) M_r must increase, followed by a decrease of β (Eq. (3.21)), weaker than the temperature rise. If this happens, Eq. (3.18) states that the temperature jump across the shock waves will be stronger, leading to more NO produced. However, at a certain point the production stops increasing, with negligible variations as p_e keeps rising. This can be attributed to the fact that the ratio p_{amb}/p_e has reached a very low value so that changes in M_r can be considered negligible, causing shock waves of almost constant intensity. Taking a closer look at the behavior at 15 km, it's possible to notice a sudden drop at around 1.4 bar. This is because of the transition to regular reflection, that occurs at lower altitude as p_e increases due to the fact that a higher M_r, as stated again by Eq. (3.21) and as visible in Fig. 3.4,

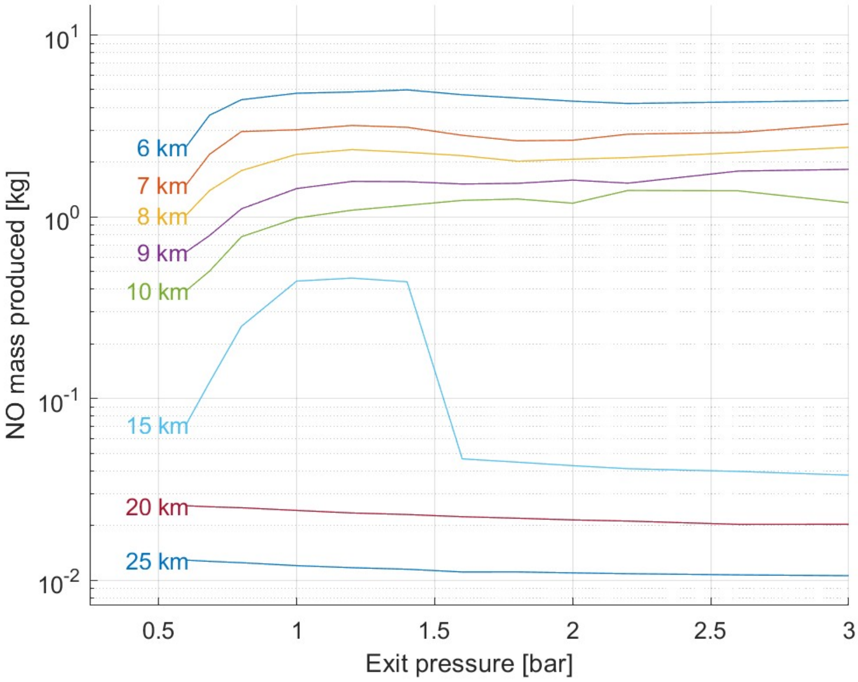

Figure 4.20: NO emissions profiles at different altitudes for different p_e

triggers a higher θ_{max} and so an earlier transition.
Eventually, in regular reflection regime, the variation of emissions appears to be very small and negligible. The reason is the same as explained before, that is, a very low value of p_{amb}/p_e.

4.4.3 Density

As shown by Figure 4.21, adopting exit density as variable with the altitude, the NO emissions decreases with increasing ρ_e from 6 km to 15 km. At 20 km and 25 km, the trend is different, with a almost constant production with increasing density.
Let's give a reason for these behaviors. CEA output for chemical species provides the mass fractions, while Eq. 3.31 is defined with the molar concentrations. This means that the mass fractions must be converted, with the following equation

$$C_j = \frac{\rho w_j}{M_j^*}$$

So, if the density increases, the molar concentrations increase.
The chemical species that exit from the nozzle are involved either in the forward and the backward reactions, O and OH for the forwards, O and H for the backward, according to Tab. 2.3 and 2.4. If the molar concentrations are higher, at fixed temperature and so fixed $k(T)$, the backward reactions become more important, inducing destruction of NO and therefore a lower estimated concentration.
As already mentioned, Zeldovich mechanism strongly depends on the temperature of the plume, which are higher with Mach reflection. So, having at 20 km and 25 km an almost constant production can be explained by the fact that the transition to regular reflection and the subsequent lower temperatures reduce the $k(T)$, and this counteracts the effect of the rise of the molar concentrations.

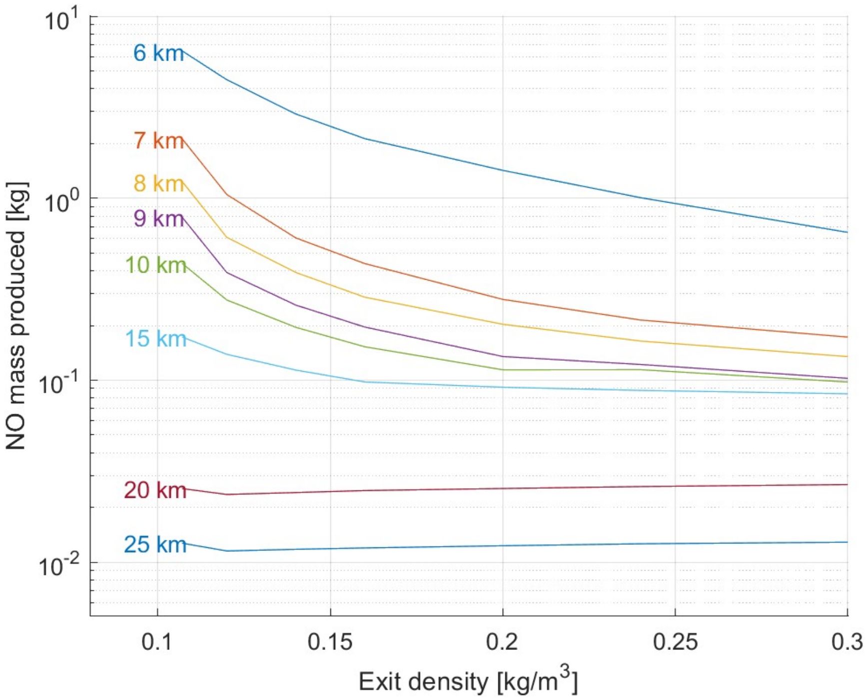

Figure 4.21: NO emissions profiles at different altitudes for different ρ_e

4.4.4 Mach number

The Figure 4.22 represents the emissions profiles for different Mach numbers at the nozzle exit and how they behave along the trajectory. Every profile, except the one at 20 km, is characterized by a monotonic increase of the emissions along the trajectory, with a decreasing slope of the curves in particular at lower altitude, which suggests that probably, for higher M_e, an asymptotic value will be reached.
These trends in the profiles can be discussed with reference to Eq. (3.13). The temperature drop across the expansion fan depends on the Mach numbers before and after the fan, resulting in a less significant cooling for a higher $M_1 = M_e$. As before, being M_r dependent only on p_{amb}, the post-shock gas will be hotter, inducing higher production of NO.

4.4.5 Nozzle diameter

With reference to Fig. 4.23, it can be seen that, as in the previous case, an increase in the considered variable leads to a monotonic increase in the NO emitted by the rocket.
The explanation has to do with the quantity of the chemical species produced. Increasing the nozzle diameter means an increase in the nozzle area. Since the mass flow rate is defined as $\dot{m} = \rho A u$, a larger diameter results in a higher mass flow. This implies that greater amounts of chemical species are present in the plume, even if the concentrations remain the same. As a result, NO formation is enhanced.

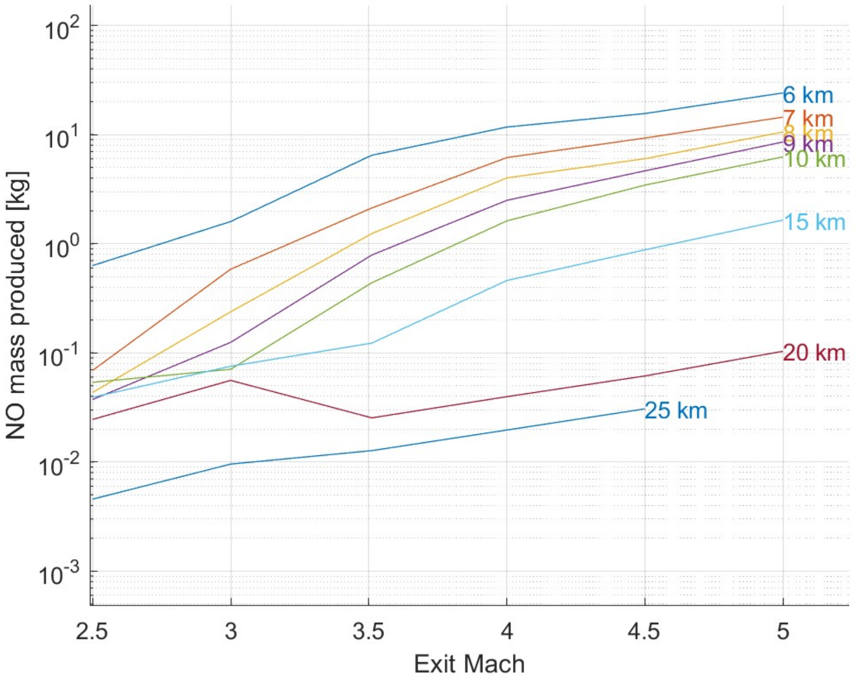

Figure 4.22: NO emissions profiles at different altitudes for different M_e

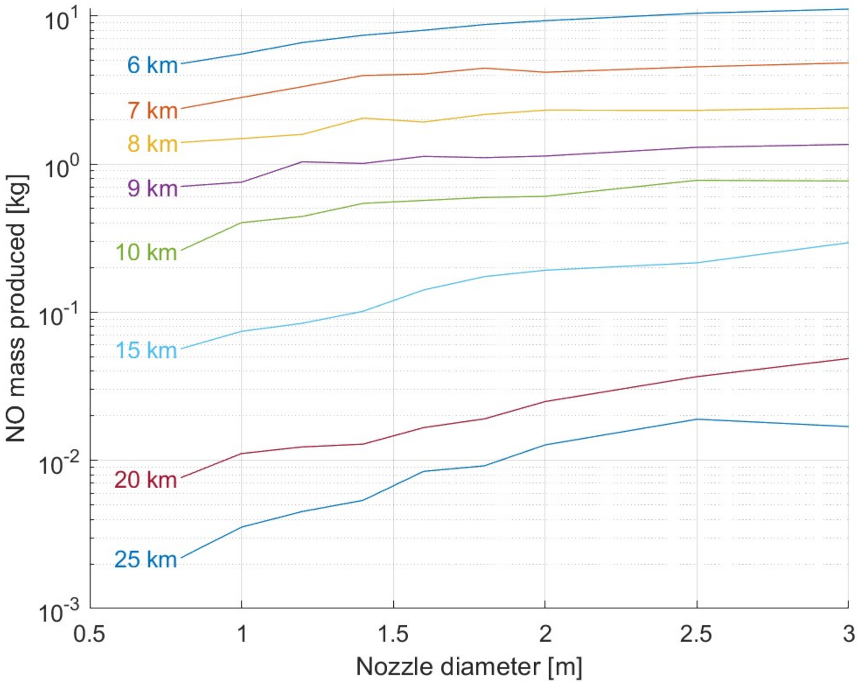

Figure 4.23: NO emissions profiles at different altitudes for different D_e

4.5 Impact of atmospheric fluctuations on emissions

The analysis goes on studying the emissions along the day and the solar cycle, to establish the influence of the atmospheric fluctuations.
As well known, the atmosphere undergoes density variations caused by

- Uneven heating of the Earth by the Sun during the day.
- Solar activity, with the absorption of Extreme Ultraviolet (EUV) and X-Ray with emitted radiations stable and at low level during the solar minimum and much higher and variable during the solar maximum.
  Solar activity is studied through the $F_{10.7}$ index, defined as *”...a measure of the solar radio flux per unit frequency at a wavelength of 10.7 cm, near the peak of the observed solar radio emission...it is an excellent indicator of overall solar activity levels and correlates well with solar UV emissions.”*, with unit of measure $1\,\mathrm{SFU} = 10^{-22}\,\mathrm{W/(m^2{\cdot}Hz)}$ (Fig. 4.24a). [15]
- Geomagnetic activity, originated by the interaction between the charged particles emitted by the Sun during solar flares and coronal mass ejections, with the Earth’s magnetosphere. These events lead to energy deposit in the atmosphere and density variations.
  Geomagnetic activity is measured through the A_p index, the averaged planetary daily of amplitude for geomagnetic activity at a specific magnetometer station (Fig. 4.24b). [16]

The solar and geomagnetic activities are strongly linked through the 11-year solar cycle. This means that during the solar maximum, radiations and emissions of charged particles are at their highest; therefore, during this period, the atmospheric density is maximum, as can be noticed in Fig. 4.25. Furthermore, the effects depend on the altitude, meaning that the thickest layers of the atmosphere are less involved, with small residual changes.

The solar cycle analyzed is the number 23, from 1996 to 2008, one of the most intense ever recorded. In Fig. 4.26, it’s possible to study its effect, noting the presence of two maxima of production in 2000 and 2004 which correspond to the maxima of atmospheric density. The 2000 maximum is characterized by elevated values of $F_{10.7}$ and A_p, respectively $F_{10.7} = 314\,\mathrm{SFU}$ and $A_p = 400$, while the 2004 maximum it’s likely linked to a delayed effect on the lower atmosphere of the October 29th 2003 geomagnetic storm. In the end, the $F_{10.7}$ maxima between late 2001 and early 2002 led to a relative minimum of NO production despite the high solar flux. This is due to the very low geomagnetic activity which counteracts the high $F_{10.7}$, leading to lower emissions.
The comparisons clearly show the relation between the NO mass emitted by the plume and the atmospheric density and therefore the O_2 and N_2 densities, which trigger the Zeldovich mechanism.

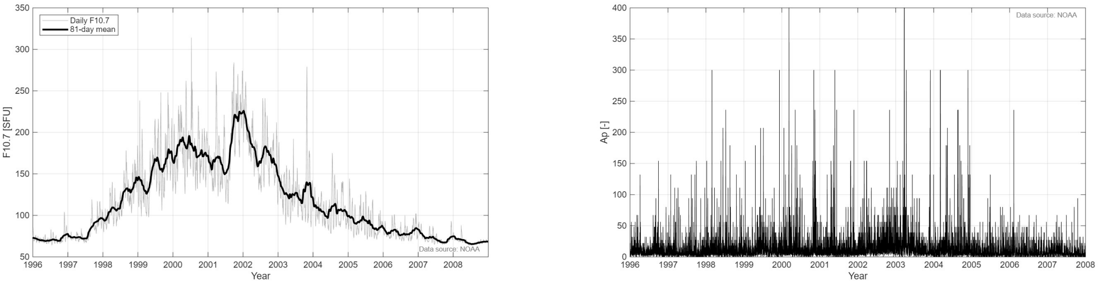

(a) Solar radio flux at 10.7 cm

(b) Geomagnetic activity

Figure 4.24: Solar activity during solar cycle 23

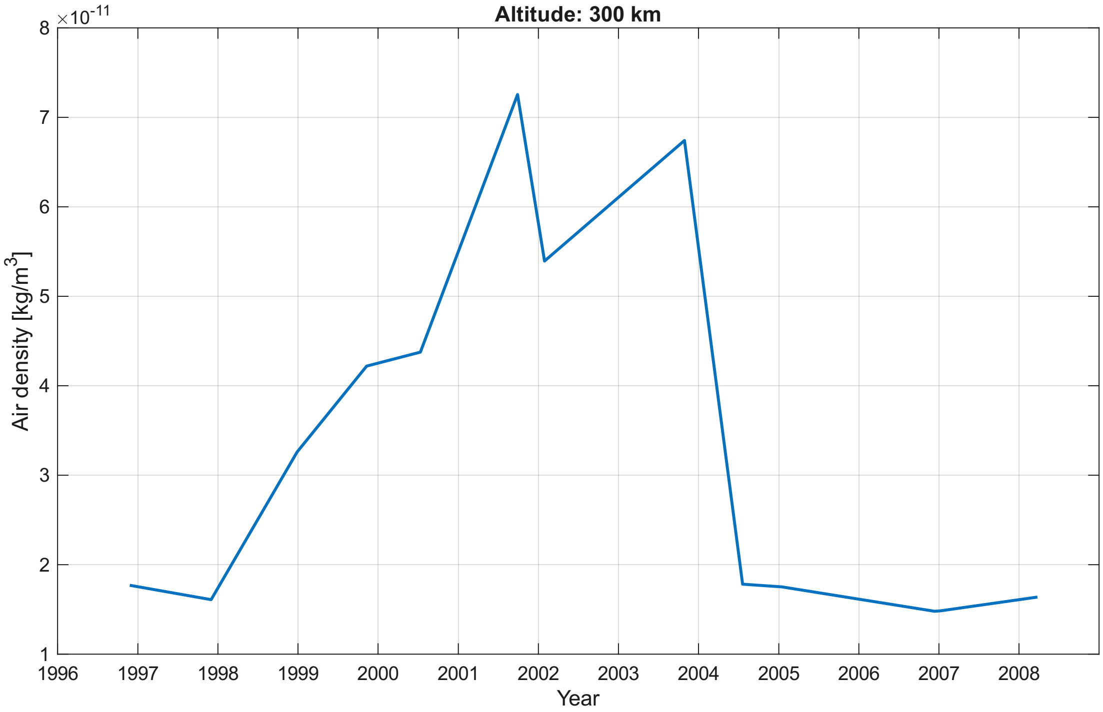

Figure 4.25: Density variation in the upper atmosphere (300 km)

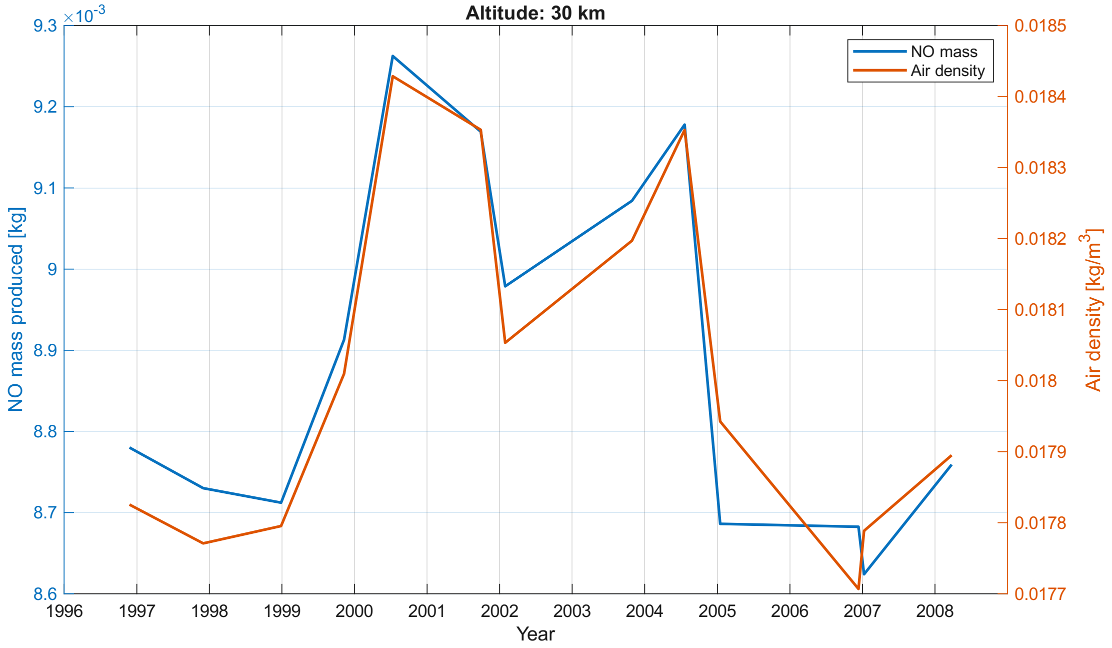

Figure 4.26: NO emissions profile along the solar cycle 23, compared with atmospheric density

4.6 Comparison between existing architectures

In this section, the emissions produced by different rocket architectures are evaluated. The selected launch vehicles and their engines have been chosen for both historical relevance and technological diversity. The configurations include different propulsion cycles, propellant combinations, and expansion ratios. The rockets considered are:

- Saturn V - F1: gas generator cycle engine, historically significant since part of Apollo program.
- Starship - Raptor 2: full-flow staged combustion engine, first of its kind, reusable.
- Ariane 6 - Vulcain 2.1: gas generator cycle engine, based on liquid hydrogen and with a high nozzle expansion ratio.
- Atlas V - RD180: staged combustion engine, characterized by a very high chamber pressure.
- Long March V - YF50: gas generator cycle engine, which uses a particular combination of propellants.

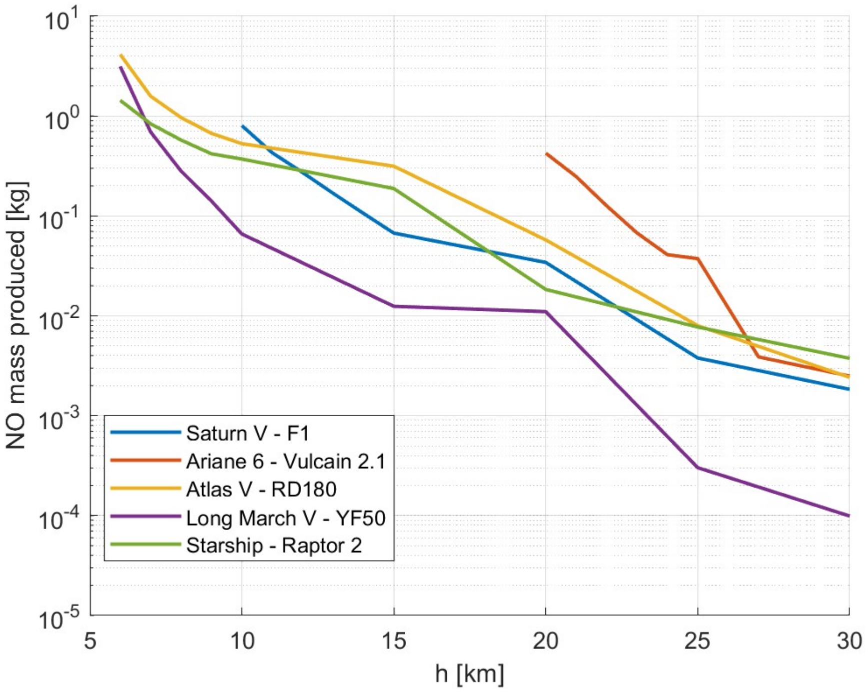

Figure 4.27: Emissions for different engine architectures

Engine	Propellants	MR	ϵ	p_c [bar]	Nozzle diameter [m]
F1	RP-1/LOX	2.27	16	70.3	1.53
Raptor 2	CH_4(L)/LOX	3.6	34.34	350	1.3
Vulcain 2.1	LH_2/LOX	6.1	58.2	120.8	2.5
RD180	RP-1/LOX	2.72	36.87	267	3.15
YF50	UDMH/N_2O_4	2	12.69	71	0.84

Table 4.1: Engines parameters

With reference to Fig. 4.27, in the case of Vulcain 2.1, it can be observed that production begins around 20 km. This behavior is due to the very low exit pressure of the gas caused by the high expansion rate (Tab. 4.1), which implies that a higher altitude is required to have an under-expanded plume, which, as already mentioned, is the plume configuration that produces more NO.

For all the engines it is clear that the transition to the regular reflection, even though for some of them it appears to be smoother, such as for RD180, which presents a more gradual decrease

Engine	M_e	p_e [bar]	T_e [K]
F1	3.548	0.48686	1716.47
Raptor 2	3.793	1.1026	2022.78
Vulcain 2.1	4.407	0.16078	1329.89
RD180	3.914	0.72762	1921.15
YF50	3.529	0.59449	1382.93

Table 4.2: Exit parameters for the engines

between 15 km and 25 km, compared to the other architectures.

An interesting case is represented by the Long March V engine. In fact, the fuel oxidizer used is N_2O_4, which triggers the production of N_2 in the nozzle and downstream within the plume, in addition to the atmospheric one. What is expected is then a larger NO mass produced, but the very low exit temperature of the flow (Tab. 4.2) counteracts the first effect, resulting in a production in line with the other architectures.

4.7 Limits of the model

The model presents some aspects that reduce its accuracy.

The first aspect to analyze is the inclination of the oblique shock waves, and in particular of the reflected shock wave. In Mach reflection, β of the reflected shock wave is in fact calculated just above the triple point, and considered constant for the entire shock wave. This is an approximation, since in reality the inclination of it continuously changes, making it a curved shock wave and not a simple oblique shock wave. This is important, since if the inclination changes, then also the Mach number of the flow crossing the shock wave changes, with a different intensity of it and a different parameters distributions along the plume.

Another limit regards the equation for the mixing layer closing angle, Eq. 3.29. Although it has been proved quite precise in estimating the desired parameter, it's limiting regarding some parametric studies, in particular with the density and the Mach number. In the first case, the term

$$s = \frac{\rho_{\text{amb}}}{\rho_{\text{pc}}}$$

can become negative. This happens when, considering the definition of ρ_{pc}

$$\rho_{\text{pc}} = 1.18\rho_{\text{e}} - 0.18\rho_{\text{amb}} < 0 => \rho_{\text{e}} < 0.1525 \cdot \rho_{\text{amb}}$$

Meaning that, if the exit density is lower than the 15.25% of the ambient density, then the equation produces a complex angle for the mixing layer, since in Eq. 3.29 there are terms $\sqrt{s}$.

In the second case, the equation considered has the term $1 - r$. r is defined as

$$r = \frac{u_{\text{amb}}}{u_{\text{pc}}}$$

so if it is bigger than 1, this means that $1-r < 0$ and the closing angle is negative and non-physical. To avoid this, $r < 1$ must be imposed, that is

$$u_{\text{amb}} < u_{\text{pc}}$$

The last aspect to take into account, that is also the most important, is the implementation of the turbulence in the mixing layer. RANS equations themselves introduce errors in the analysis of the turbulence, due to the closure models and the fact that they substitute a very complex phenomenon with mean quantities. The errors introduced can be up to 20%. In addition to this, the finite difference method used for approximating the equations, accompanied by the least square method, further increases the error in the simulation.

The known limitations of RANS modeling become more evident in the presence of strong pressure and velocity gradients, as in rocket plumes. In these conditions the turbulence model may not accurately represent the flow physics, and when combined with the strong nonlinearities of the governing equations this can lead to numerical difficulties and reduced accuracy due to the amplification of the already existing errors. This behavior can be observed by analyzing the spatial residuals of the equations (Fig. 4.28). Although the residual levels remain very small, reaching values on the order of 10^{-12}, the residuals of the x- and y-momentum equations exhibit strong oscillations along the domain.

By the way, it's important to note that low residual norms do not necessarily imply high physical accuracy, especially in the presence of strong gradients and nonlinearities, where the model and numerical errors may still be significant.

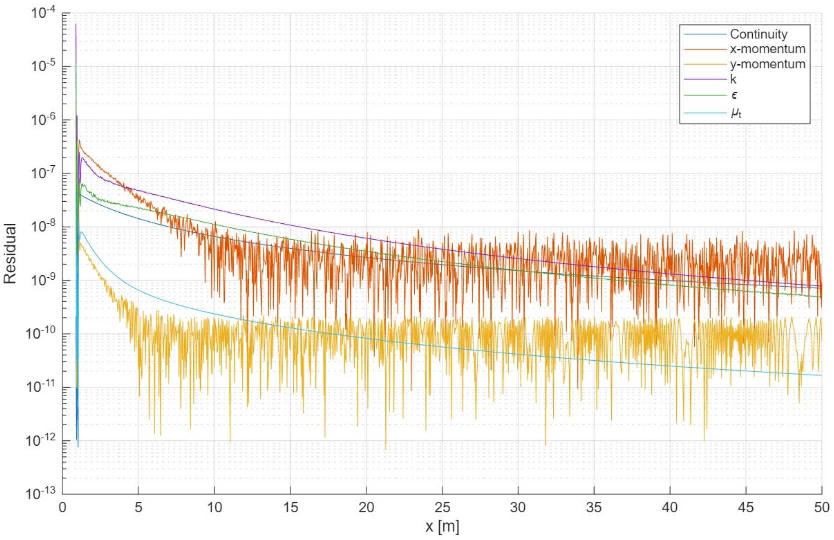

Figure 4.28: Residuals for the RANS equations

In general, the structure of the code presents aspects that limit the field of application, for example altitudes very close to the point where there is a transition from an over-expanded plume to an under-expanded plume or at very high altitudes generate errors. Another example is the use of some of the MATLAB existing function, such as `fsolve`, adopted for the solution of transcendental equations, which requires an initial point. The MATLAB Help Center cites "...fzero(fun,x0) tries to find a point x where fun(x) = 0. This solution is where fun(x) changes sign...", meaning that, if the sign change doesn't occur, the function doesn't calculate the requested value and the entire code is blocked. [17]

5 Summary

In this thesis, the interaction between the rocket plume and the surrounding atmosphere has been studied. The approach has consisted on a introductory part regarding the problem and the goals of the thesis, followed by an explanation of the main pollutants produced within the plume and the nozzle and their environmental impact in terms of warming up the atmosphere. These are soot, also known as black carbon, alumina Al_2O_3 and nitrogen oxide NO.
The plume structure has then been analyzed, with particular attention paid to the shock waves and their reflection, the expansion fan at the nozzle exit and the turbulence in the mixing layer. The last one, in particular, is fundamental for fulfilling the main goal of the thesis: the estimation of NO production due to the Zeldovich mechanism. This process is part of the so-called afterburning, that leads also to the soot oxidation, which produces CO and, in smaller part, CO_2.
Once all the theoretical part has been introduced, a model must be implemented. This consists on basic governing equations, Rankine-Hugoniot relations for shock waves, Prandtl-Meyer theory for expansion fan, RANS equations with closure model $k-\epsilon$ for the mixing layer and the chemical reactions equations. These are solved analytically or, for example in the case of RANS, through numerical methods.
One of the Section of the thesis has also been dedicated to the exposition of the implementation of the model and its description in MATLAB, with the functions created and how they are linked together, creating a functional code for solving the plume structure in terms of velocity, temperature, pressure and density.
At this point, the results from the model were analyzed. First of all, the entire plume structure has been examined with the distribution of Mach number, temperature and pressure, with a clear distinction between the Mach reflection and regular reflection regimes and their peculiar characteristics. Later, the investigation of the NO production for a general rocket engine has been conducted, first checking the general behavior with changing altitude, and then comparing the emissions in the case of equilibrium composition and frozen composition of the gas in the nozzle. Subsequently, once established the worst case scenario, that is the equilibrium composition, a parametric study of the NO produced has been conducted, evaluating how it changes for different altitude, for different temperatures, pressures and Mach numbers at the nozzle exit, and for different nozzle diameters. In the end, a comparison between the environmental impact of existing engine architecture, chosen for both historical relevance and technological diversity, was conducted.
Specifically, it has been noted the following

- Temperature: an increase in the exit temperature does not lead to a monotonic increment of the NO mass, since at a certain value there is a changing in the main production process, that is from the Zeldovich mechanism to the reaction between the extremely reactive radicals N and O.
- Pressure: increasing the exit pressure triggers an increase of the NO estimated till an asymptotic value of production is reached at every altitude, caused by the fact that $p_{\mathrm{amb}}/p_{\mathrm{e}}$ is very low and the Mach number at the reflection point is almost constant.
- Density: a rise in the exit density leads to a decrease of the production in Mach reflection regime, since an higher density means an higher molar concentration of the chemical species,

making the backward reactions more and more important and therefore reducing the effect of the forward reactions. In regular reflection, the lower temperatures reduce the constant velocities $k(T)$, counteracting the effect of the molar concentration and causing a plateau in the production plot for higher altitudes.

- Mach number: a faster flow at the nozzle exit results in a less significant cooling of the gas, inducing a hotter post-shock flow and so a higher NO production.
- Nozzle diameter: at fixed exit velocity, a bigger nozzle exit area means a higher mass flow rate and greater amounts of chemical species in the plume which enhance the NO formation.

In the end, an analysis of the model limits has been carried on, identifying in some approximations, the equation for the mixing layer closing angle and the turbulence implementation critical aspects for the accuracy.

Based on the results obtained, several improvements are proposed to enhance the model accuracy and reliability. More precisely, as regards the mixing layer, a shift from the $k - \epsilon$ model to the Menter's Shear Stress Transport (SST) model may introduce a better prediction of the shear layer, thanks to a bigger accuracy in presence of high velocity and temperature gradients. Another improvement could be the use of the Finite Volume Method (FVM) instead of finite difference methods, which is used by all the professional CFD solver. In the end, since the typical very high temperatures within the plume, the hypothesis of calorically perfect gas may be changed, considering c_v and c_p not indipendent anymore from the temperature.

Bibliography

[1] McDowell, J. C.: *General Catalog of Artificial Space Objects, Release 1.5.7.* `https://planet4589.org/space/gcat`. Accessed: 2025-01-13. 2020.

[2] Fischer, J.-S.; Fasoulas, S.: "Review of the environmental impact of space transportation systems towards a full life cycle assessment". In: *73rd International Astronautical Congress (IAC), Paris, France.* 2022, pp. 18–22.

[3] Dallas, J. et al.: "The environmental impact of emissions from space launches: A comprehensive review". In: *Journal of Cleaner Production* 255 (2020), p. 120209.

[4] Ross, M.; Vedda, J.: "The Policy and Science of Rocket Emissions". In: *Journal of Space Policy* (Apr. 2018), pp. –.

[5] Glarborg, P. et al.: "Modeling nitrogen chemistry in combustion". In: *Progress in energy and combustion science* 67 (2018), pp. 31–68.

[6] Hill, S.; Smoot, L. D.: "Modeling of nitrogen oxides formation and destruction in combustion systems". In: *Progress in energy and combustion science* 26.4-6 (2000), pp. 417–458.

[7] Baulch, D. L. et al.: "Evaluated kinetic data for combustion modelling. Supplement I". In: *Journal of Physical and Chemical Reference Data* 23 (1994). Squib: 1994BAU/COB847-1033, pp. 847–1033.

[8] Molina, M. J. et al.: "The reaction of ClONO2 with HCl on aluminum oxide". In: *Geophysical Research Letters* 24.13 (1997), pp. 1619–1622.

[9] The Space Techie: *Testing - The Space Techie.* Accessed: 2025-07-08. 2024. URL: `https://www.thespacetechie.com/category/testing/`.

[10] Jadidi, M.; Moghtadernejad, S.; Dolatabadi, A.: "A comprehensive review on fluid dynamics and transport of suspension/liquid droplets and particles in high-velocity oxygen-fuel (HVOF) thermal spray". In: *Coatings* 5.4 (2015), pp. 576–645.

[11] Bauer, C. et al.: "Engineering model for rocket exhaust plumes verified by CFD results". In: (2013).

[12] Viswanath, K. et al.: "Investigation of soot combustion in underexpanded jet plume flows". In: *Journal of thermophysics and heat transfer* 19.3 (2005), pp. 282–293.

[13] Simmons, F.: *Rocket exhaust plume phenomenology.* American Institute of Aeronautics and Astronautics, Inc., 2000.

[14] National Oceanic and Atmospheric Administration (NOAA): *National Oceanic and Atmospheric Administration Homepage.* U.S. Department of Commerce. URL: `https://www.noaa.gov/`.

[15] Wikipedia contributors: *Solar cycle — Wikipedia, The Free Encyclopedia.* `https://en.wikipedia.org/wiki/Solar_cycle`. 2024.

[16] Wikipedia contributors: *K-index — Wikipedia, The Free Encyclopedia.* `https://en.wikipedia.org/wiki/K-index`. 2024.

[17] The MathWorks, I.: *fzero - Root of nonlinear function.* `https://it.mathworks.com/help/matlab/ref/fzero.html`. 2024.